

The core spliceosome as target and effector of non-canonical ATM signalling

Maria Tresini¹, Daniël O. Warmerdam², Petros Kolovos³, Loes Snijder¹, Mischa G. Vrouwe⁴, Jeroen A. A. Demmers⁵, Wilfred F. J. van IJcken⁶, Frank G. Grosveld³, René H. Medema², Jan H. J. Hoeijmakers¹, Leon H. F. Mullenders⁴, Wim Vermeulen¹ & Jurgen A. Marteijn¹

In response to DNA damage, tissue homeostasis is ensured by protein networks promoting DNA repair, cell cycle arrest or apoptosis. DNA damage response signalling pathways coordinate these processes, partly by propagating gene-expression-modulating signals. DNA damage influences not only the abundance of messenger RNAs, but also their coding information through alternative splicing. Here we show that transcription-blocking DNA lesions promote chromatin displacement of late-stage spliceosomes and initiate a positive feedback loop centred on the signalling kinase ATM. We propose that initial spliceosome displacement and subsequent R-loop formation is triggered by pausing of RNA polymerase at DNA lesions. In turn, R-loops activate ATM, which signals to impede spliceosome organization further and augment ultraviolet-irradiation-triggered alternative splicing at the genome-wide level. Our findings define R-loop-dependent ATM activation by transcription-blocking lesions as an important event in the DNA damage response of non-replicating cells, and highlight a key role for spliceosome displacement in this process.

The DNA damage response (DDR), an intricate protein network that promotes DNA repair, translesion synthesis, cell cycle arrest or apoptosis, has evolved to counteract the detrimental effects of DNA lesions^{1–3}. At the core of the DDR, the ataxia telangiectasia mutated (ATM) and ataxia telangiectasia and Rad3-related (ATR) signalling pathways coordinate these processes in response to distinct types of DNA damage: ATR to single-stranded DNA damage, and ATM to double-strand DNA breaks (DSBs) and chromatin modifications^{1,4,5}. These signalling networks utilize post-translational modifications and protein–protein interactions to elicit the initial stages of the cellular response. Later DDR stages involve changes in gene expression. Emerging evidence supports that DNA damage influences not only the expression levels of its target genes, by altering transcription rates and mRNA half-life, but also exon selection and ultimately their coding potential⁶.

Production of mature, protein-coding transcripts depends on the selective intron removal catalysed by the spliceosome, a dynamic ribonucleoprotein complex consisting of five small nuclear ribonucleoprotein (snRNP) complexes (U1, U2, U4, U5 and U6), and a large number of accessory proteins^{7,8}. Exon/intron definition by U1 and U2 snRNPs stimulates the recruitment of the pre-assembled U4/U6.U5 tri-snRNP and numerous non-snRNP proteins. Following U1/U4 displacement and extensive conformational rearrangements, the two-step splicing reaction is catalysed by the mature, catalytically active spliceosome composed of U2, U5 and U6 snRNPs⁸.

The vast majority of mammalian genes are alternatively spliced to produce multiple mRNA variants from a single gene⁹, thus expanding protein diversity. Numerous mechanisms have evolved to provide the spliceosome with the plasticity required for selective exon inclusion, without compromising splicing fidelity⁹. These range from the presence of *cis*-acting elements on the transcript itself to post-translational modifications of spliceosomal proteins, which are subject to intracellular and environmental cues. Additionally, since most introns are

spliced co-transcriptionally within the chromatin environment, splicing decisions are subject to spatiotemporal control imposed by transcribing polymerases and interaction with chromatin remodellers and histone marks^{10–12}. Exon selection is also influenced by DNA damage^{6,13}. There is evidence for a broad range of damage-induced alternative splicing events, including alternative exon inclusion and exon skipping, and production of proteins with altered (often pro-apoptotic) function^{13–16}. DNA-damage-induced alternative splicing has been attributed to changes in the processivity rate of RNA polymerase¹⁶ (kinetic coupling), or changes in the interactions between the polymerase and splicing regulators^{14,15} (recruitment coupling), under the assumption that the core spliceosome is largely unaffected. Here we present evidence that DNA damage triggers specific profound changes in spliceosome organization, primarily that of late-stage spliceosomes. Additionally, we identify reciprocal regulation between ATM-controlled DDR signalling and the core spliceosome, and show that in response to transcription-blocking DNA lesions, non-canonical ATM activation contributes to the selection of genetic information ultimately included in mature transcripts.

DNA damage targets core spliceosomes

To gain mechanistic insight on the influence of DNA damage to chromatin-associated DDR processes, we used stable isotope labelling with amino acids in cell culture (SILAC)-based quantitative proteomic analysis¹⁷ to characterize ultraviolet (UV)-irradiation-triggered changes in chromatin composition (Extended Data Fig. 1a–c). Indirect effects of replication stress were avoided by use of quiescent, human dermal fibroblasts (HDFs). UV-induced photolesions inhibit transcription by impeding RNAPII progression, and as anticipated we observed a UV-dependent chromatin-depletion of core splicing factors. Surprisingly though, this depletion was selective; chromatin abundance of all detected U2 and U5 snRNP splicing factors was

¹Department of Genetics, Cancer Genomics Netherlands, Erasmus University Medical Center, Rotterdam, 3015 CN, The Netherlands. ²Division of Cell Biology, Netherlands Cancer Institute, Amsterdam, 1066 CX, The Netherlands. ³Department of Cell Biology, Erasmus University Medical Center, Rotterdam, 3015 CN, The Netherlands. ⁴Department of Human Genetics, Leiden University Medical Center, Leiden, 2333 ZC, The Netherlands. ⁵Erasmus MC Proteomics Center, Erasmus University Medical Center, Rotterdam, 3015 CN, The Netherlands. ⁶Erasmus Center for Biomics, Erasmus University Medical Center, Rotterdam, 3015 CN, The Netherlands.

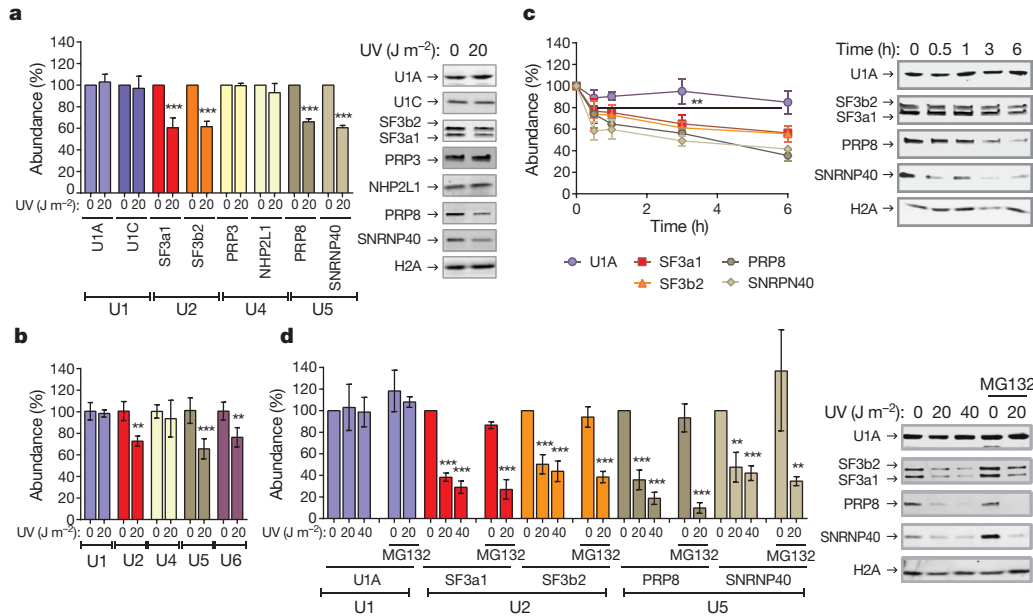


Figure 1 | DNA-damage-triggered chromatin displacement of activated spliceosomes. **a, b,** UV-induced changes in chromatin association of spliceosome components in quiescent HDFs. **a,** Immunoblots (right) and quantification (left) of splicing factor–chromatin association. **b,** Chromatin-associated snRNAs assayed by quantitative PCR (qPCR) and normalized to HotAir non-coding RNA ($n = 4$, mean \pm s.d., t -test). **c, d,** Immunoblots (right)

and quantification (left) of splicing factor–chromatin association in U2OS cells. **c,** Time post UV irradiation. **d,** UV dose-response and lack of influence of the proteasome inhibitor MG132. Graphs in **c, d** show signal intensities normalized to H2A ($n = 3$, mean \pm s.d., t -test and one-way ANOVA). ** $P < 0.01$, *** $P < 0.001$.

substantially decreased in irradiated cells while abundance of U1 and U4 snRNP splicing factors was not significantly affected (Extended Data Fig. 1d and Supplementary Table 1). Considering that spliceosomes containing exclusively U2/U5/U6 snRNPs are formed at later stages of the splicing cycle, following eviction of U1 and U4 from the assembled spliceosome⁸, we concluded that DNA damage preferentially targets late-maturation-stage spliceosomes, unlike chemical transcription inhibition that also affects early-stage spliceosome assembly¹⁸.

The proteomic results were validated by chromatin fractionation and immunoblotting, for U1 (U1A, U1C), U2 (SF3a1, SF3b2), U4 (PRP3, NHP2L1) and U5 (SNRNP40, PRP8) snRNP-specific proteins⁸ (Fig. 1a). We also assayed by qPCR the chromatin association of all spliceosomal snRNAs. UV irradiation resulted in preferential chromatin depletion of U2, U5 and U6 snRNAs, while U1 and U4 were essentially unaffected (Fig. 1b). Depletion of U2 and U5 snRNP proteins was time- (Fig. 1c) and dose-dependent (Fig. 1d), but independent of proliferation status and cell type (Fig. 1a, c, d). Chromatin-depletion of U2 and U5 snRNP splicing factors was independent of proteasome activity (Fig. 1d), suggesting that depletion was not caused by splicing factor degradation but rather by relocalization. In agreement, total cellular levels of all tested splicing factors were unaffected by DNA damage (Extended Data Fig. 1e). Splicing factor relocalization was verified by immunofluorescence microscopy in cells in which DNA damage was inflicted in a small subnuclear area. A representative example in Fig. 2a depicts depletion of the U5-associated protein SNRNP40 from DNA damage sites that were identified by cyclobutane pyrimidine dimer (CPD) immunodetection¹⁹. Re-localization was monitored in real-time, using validated cell lines (Extended Data Fig. 2a–d) stably expressing GFP-tagged members of U2 (SF3a1) and U5 (SNRNP40, PRP8) snRNPs. Subnuclear damage infliction by UVC microbeam irradiation¹⁹ resulted in rapid depletion from irradiated sites of GFP-tagged U2 and U5 snRNP splicing factors but not of U1 and U4 (Fig. 2b and Extended Data Fig. 3a–c). Inhibition of transcription-initiation prevented this depletion indicating that the displaced proteins were actively involved in splicing (Extended Data Fig. 3d). Irradiation of the entire cell resulted in prominent changes in splicing factor localization as evi-

denced by speckle reorganization and enlargement (Extended Data Fig. 4a, b). To further investigate the relocalization kinetics of GFP-tagged SFs, we measured their mobility by fluorescence recovery after photobleaching (FRAP). We observed substantial and UV-dose-dependent increases in the mobility of U2 and U5 snRNP factors

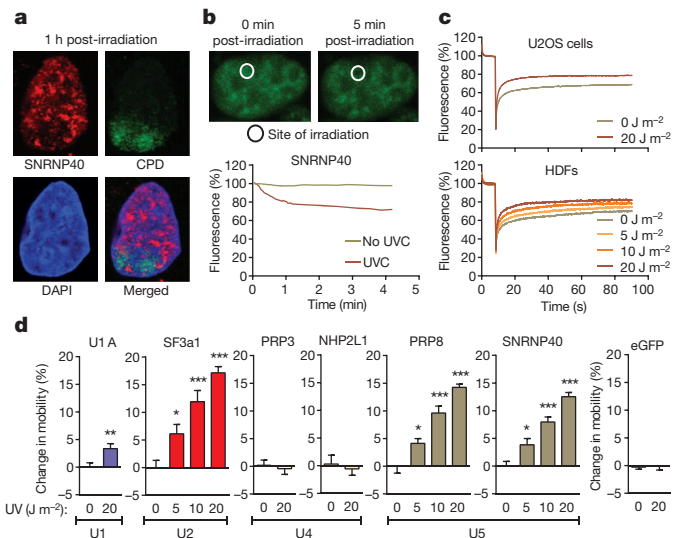


Figure 2 | Mobilization and displacement of mature spliceosomes from sites of UVC-induced DNA damage. **a,** Immunofluorescence detection of SNRNP40 and CPDs in U2OS cells exposed to UV irradiation through porous membranes. **b,** SNRNP40–GFP depletion from UVC laser microbeam irradiation sites in U2OS cells; typical image (top) and fluorescence quantification of 20 cells (bottom). **a, b,** Images were obtained at 63 \times magnification. **c,** FRAP of UV-triggered SNRNP40–GFP mobilization in U2OS and quiescent HDFs ($n = 25$). **d,** FRAP of free eGFP or GFP-tagged splicing factors in UV-irradiated quiescent HDFs. Change in mobility was calculated as the fluorescence of irradiated cells – fluorescence of non-irradiated cells at 1 min post-bleaching ($n = 25$, mean \pm s.e.m., t -test and one-way ANOVA). * $P < 0.05$, ** $P < 0.01$, *** $P < 0.001$.

but not of U1 and U4, at 1 hour post-irradiation (Fig. 2c, d). In agreement with the chromatin fractionation assays (Fig. 1d), mobilization was independent of proteasome activity, confirming that the UV-triggered mobilization is not caused by proteasome-dependent degradation (Extended Data Fig. 5d).

The UV-dependent chromatin depletion of snRNAs and proteins participating in late-stage spliceosomes, loss of association with elongating RNAPII (Extended Data Fig. 1f), rapid displacement from DNA damage sites and mobilization of U2 and U5 snRNP factors, indicate that UV irradiation influences late-stage RNAPII-associated spliceosomes.

DNA-damage-specific spliceosome mobilization

Next we used FRAP to address whether spliceosome mobilization is caused by specific DNA lesions or is a general response to macromolecular damage. Significant splicing factor mobilization was caused by genotoxins inflicting transcription-blocking DNA lesions (UV irradiation, Illudin S), but not oxidative damage (tert-butyl-hydroxide, rotenone, ionizing radiation), DSBs (ionizing radiation) or DNA inter-strand crosslinks (mitomycin C). This specificity argues that the observed mobilization does not result from non-specific RNA/DNA damage but only from DNA lesions that interrupt transcription (Fig. 3a and Extended Data Fig. 5a, b) and are substrates of the transcription-coupled nucleotide excision repair (TC-NER) pathway^{20,21}. Notably, HDFs deficient in either TC-NER, or global-genome (GG)-NER (lacking CSB and XPC activities respectively), or in both (lacking XPA), show no impairments either in damage-triggered spliceosome mobilization (Fig. 3b) or in chromatin-displacement of endogenous U2 and U5 snRNP splicing factors (Extended Data Fig. 5c). Thus, the influence of transcription-blocking lesions in splicing factor localization is independent from NER complex assembly indicating that pausing of elongating RNAPII is necessary and sufficient to trigger chromatin displacement of late-stage spliceosomes.

Spliceosome mobilization by DDR signals

Transcription inhibition by chemicals that target RNAPII mobilize splicing factors of all snRNPs, unlike UV irradiation that preferentially targets those participating in late-stage complexes (Fig. 4b

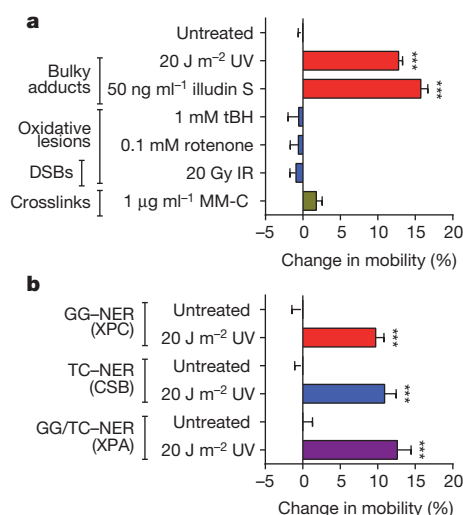


Figure 3 | Chromatin displacement of mature spliceosomes is caused by RNAPII-blocking lesions and is NER-independent. **a**, FRAP of SNRNP40-GFP in quiescent HDFs exposed to genotoxins ($n = 30$, mean \pm s.e.m., one-way ANOVA). IR, ionizing radiation; tBH, tert-butylhydroperoxide; MM-C, mitomycin-C. **b**, UV-triggered mobilization of SNRNP40-GFP in HDFs deficient in GG-NER (XPC), TC-NER (CSB) or both (XPA) ($n = 30$, mean \pm s.e.m., t -test). *** $P < 0.001$.

and Extended Data Fig. 5e). This preferential mobilization implies distinct mechanisms of action between UV-irradiation-dependent and chemically-induced transcription inhibition. However, to formally exclude the possibility that transcription-blocking DNA lesions mobilize spliceosomes exclusively through RNAPII arrest, we used 5,6-dichloro-1- β -D-ribofuranosyl-benzimidazole (DRB) to inhibit transcription to the same extent as UV irradiation. Transcription arrest was evaluated by measuring reduced 5-ethynyl-uridine (5EU) incorporation into newly synthesized RNA (Fig. 4a). Both treatments increased spliceosome mobility (Fig. 4b and Extended Data Fig. 6a) and their combination had an additive effect (Extended Data Fig. 6b). Notably, UV irradiation had a more profound splicing-factor-mobilizing effect than DRB (at equal transcription-inhibiting doses), indicating that transcription inhibition alone is not sufficient to attain the extensive mobilization triggered by UV irradiation (Fig. 4b and Extended Data Fig. 6a).

Pausing of RNAPII at DNA lesions not only halts transcription, but also activates DDR signalling pathways that modulate the cellular response via post-translational modifications^{1,22}. Considering that many core splicing factors have been identified as DDR-kinase substrates^{22,23}, we used the broad-range DDR-kinase inhibitor caffeine to evaluate if DDR signalling influences spliceosome organization. Caffeine partially suppressed the UV-dependent spliceosome mobilization but had no influence on the DRB-dependent mobilization, confirming that the two processes are, in part, mechanistically distinct (Fig. 4d).

To dissect which DDR signalling system augments the UV-triggered spliceosome mobilization, cells were treated with specific inhibitors of the major caffeine-sensitive DDR kinases: ATM, ATR and DNA-dependant protein kinase (DNA-PK). Neither ATR nor DNA-PK inhibition had a significant effect (Fig. 4c and Extended Data Fig. 6d). Surprisingly, ATM inhibition in non-replicating cells suppressed splicing factor mobilization to levels similar to caffeine (Fig. 4c and Extended Data Fig. 6d), while it had no influence on DRB-mediated mobilization (Extended Data Fig. 6h). The dependency of UV-triggered spliceosome mobilization on ATM signalling was confirmed by the impaired splicing factor mobilization in HDFs derived from an ataxia telangiectasia patient compared to those of a healthy donor (Fig. 4e and Extended Data Fig. 6c). Thus DNA-damage-triggered spliceosome mobilization results from the combined contribution of transcription inhibition and ATM signalling.

To evaluate the impact of ATM-dependent spliceosome mobilization on pre-mRNA processing, we assayed splicing efficiency in a select panel of DDR- and cell-cycle-related genes²⁴. Quiescent RPE cells were UV irradiated in the absence or presence of the ATM inhibitor and intron retention was assayed by reverse-transcription PCR (RT-PCR)²⁴. UV irradiation resulted in increased ATM-dependent intron retention (Fig. 4f and Extended Data Fig. 6f), while transcription inhibition by DRB had minor, and ATM-independent, effects. Specificity of the ATM inhibitor was confirmed by small-interfering RNA (siRNA)-mediated ATM silencing which gave identical results (Extended Data Fig. 6e).

To investigate the genome-wide influence of UV irradiation on alternative splicing, as well as the ATM contribution in UV-irradiation-dependent gene expression and mRNA processing changes, we performed RNA sequencing (RNA-seq) on cells that were untreated or UV-irradiated in the presence or absence of the ATM inhibitor. We observed that a substantial number of UV-induced gene expression changes depend on ATM activity (Extended Data Fig. 6g), revealing a previously unknown contribution of ATM signalling in the UV-regulated transcriptome. Importantly, UV irradiation resulted in widespread splicing changes, a subset of which (up to 40%) was partly ATM-dependent, demonstrating the genome-wide influence of ATM not only in mRNA abundance but also in UV-induced alternative splicing (Fig. 4g and Supplementary Table 2).

Collectively, these findings demonstrate that UV irradiation influences gene expression in an ATM-dependent manner, and that ATM

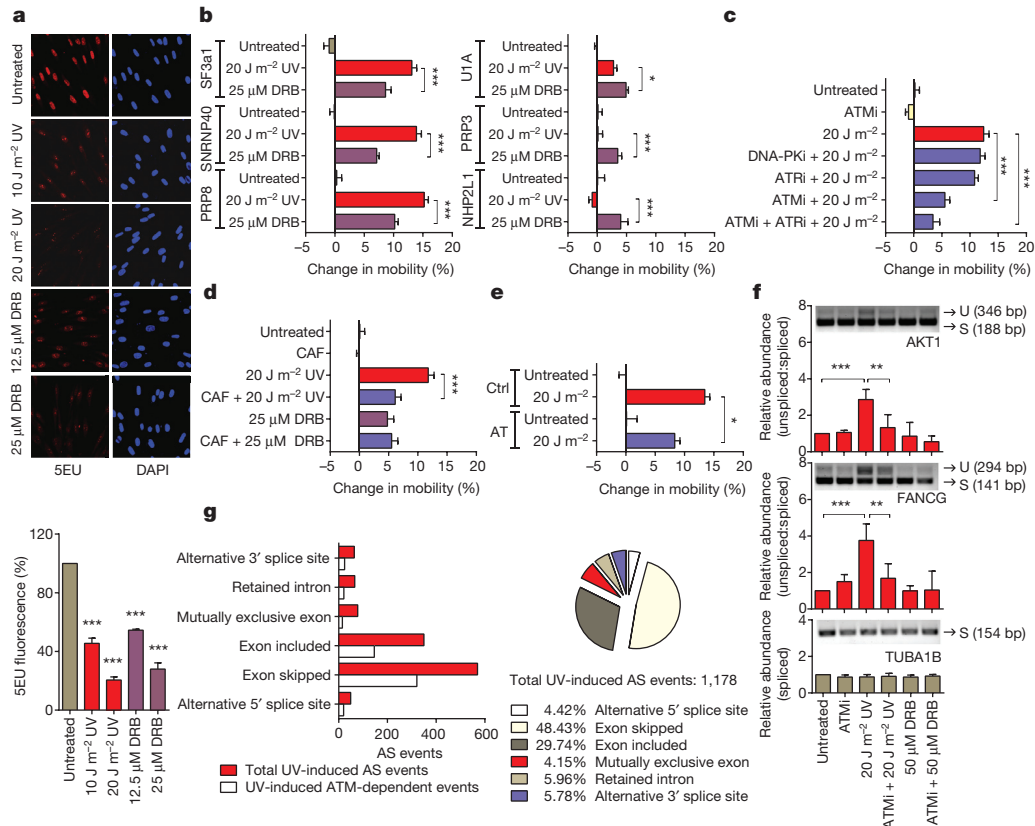


Figure 4 | ATM modulates spliceosome mobilization and influences splicing decisions upon DNA damage. **a**, RNA synthesis measured by 5EU pulse labelling ($n = 150$, mean \pm s.e.m., t -test). Top, representative images obtained at 20 \times magnification. Bottom, graph of quantification ($n = 150$, mean \pm s.e.m., t -test). **b–e**, FRAP of splicing factors in quiescent HDFs ($n = 25$, mean \pm s.e.m., one-way ANOVA). **b**, Response to UV or DRB treatment. **c–e**, SNRNP40 response to: **c**, UV irradiation with or without ATM, ATR or DNA-PK inhibitors (ATMi, ATRi and DNA-PKi, respectively); **d**, UV or DRB

participates in the selection of the genetic information contained in mature transcripts, thus revealing a novel non-canonical function of ATM in DDR.

Spliceosome–ATM reciprocal regulation

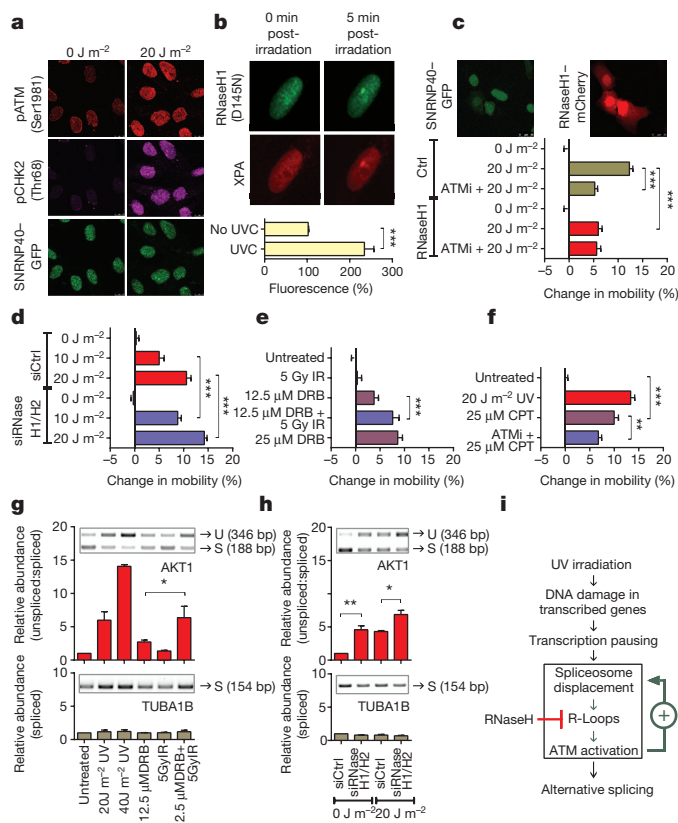
The ATM-dependency of splicing-factor-mobilization in quiescent cells indicates that UV irradiation activates ATM via a mechanism distinct from its canonical activation by replicative-stress- and ionizing-radiation-inflicted DSBs^{4,25}. UV irradiation of quiescent HDFs activated ATM, as evidenced by its auto-phosphorylation²⁶ and phosphorylation of CHK2²⁷ (Fig. 5a and Extended Data Fig. 7a–e) to levels similar to the topoisomerase I inhibitor camptothecin (CPT)²⁸ and the deacetylase inhibitor and non-canonical ATM activator, trichostatin A (TSA)⁵ (Extended Data Fig. 7a). Notably, in UV-irradiated cells active ATM was dispersed throughout the nucleus, which contrasts to the focal accumulation triggered by DSB-inducing agents such as CPT or ionizing radiation (Extended Data Fig. 7e). Furthermore, in cells where ATR was also inhibited²⁹, UV-dependent γ H2AX and 53BP1 foci were rare (Extended Data Fig. 7f), suggesting that in non-proliferating cells UV-dependent ATM activation occurs in the absence of DSBs.

Impairments in co-transcriptional splicing promote hybridization of nascent RNA and single-stranded template DNA at the transcription bubble, resulting in three-nucleic-acid-strand structures known as R-loops²⁵. R-loops have been reported to cause genomic instability after splicing factor depletion^{25,30} and activate ATM in both proliferating and post-mitotic cells^{28,31}. In agreement, siRNA-mediated silencing of

U2 or U5 snRNP splicing factors, or combined RNase H1/H2A silencing, resulted in ATM activation in the absence of other treatments (Extended Data Fig. 8a, b, g). Similarly, treatment of quiescent cells with pladienolide B³², which arrests late-stage spliceosomes and mobilizes U5, and to a lesser extent U2 snRNP splicing factors (Extended Data Fig. 8c), resulted in robust ATM activation (Extended Data Fig. 8d, e) and intron-retention levels comparable to UV irradiation (Extended Data Fig. 8f). To explain our observations we formulated the following hypothesis: RNAPII arrest at DNA lesions displaces a subset of splicing factors engaged in co-transcriptional splicing. Spliceosome displacement, in combination with negative supercoiling behind RNAPII, facilitates hybridization of naked pre-mRNA (still containing intronic sequences) to the DNA template strand. The resulting R-loop activates ATM, which then amplifies the mobilization signal and stimulates further spliceosome displacement either by promoting disassembly or preventing assembly of late-stage spliceosomes. Accordingly, we predicted that: (1) R-loops are formed at sites of UV-induced DNA damage; and (2) manipulation of R-loop levels will alter spliceosome mobility.

U2 or U5 snRNP splicing factors, or combined RNase H1/H2A silencing, resulted in ATM activation in the absence of other treatments (Extended Data Fig. 8a, b, g). Similarly, treatment of quiescent cells with pladienolide B³², which arrests late-stage spliceosomes and mobilizes U5, and to a lesser extent U2 snRNP splicing factors (Extended Data Fig. 8c), resulted in robust ATM activation (Extended Data Fig. 8d, e) and intron-retention levels comparable to UV irradiation (Extended Data Fig. 8f). To explain our observations we formulated the following hypothesis: RNAPII arrest at DNA lesions displaces a subset of splicing factors engaged in co-transcriptional splicing. Spliceosome displacement, in combination with negative supercoiling behind RNAPII, facilitates hybridization of naked pre-mRNA (still containing intronic sequences) to the DNA template strand. The resulting R-loop activates ATM, which then amplifies the mobilization signal and stimulates further spliceosome displacement either by promoting disassembly or preventing assembly of late-stage spliceosomes. Accordingly, we predicted that: (1) R-loops are formed at sites of UV-induced DNA damage; and (2) manipulation of R-loop levels will alter spliceosome mobility.

To visualize and resolve R-loops in UV-irradiated cells we exploited the ability of RNaseH to bind and hydrolyse RNA at RNA–DNA duplexes³³. For indirect, real-time visualization of R-loops, we used HDFs stably expressing GFP-tagged RNaseH1(D145N), a binding-competent but catalytically inactive RNaseH1³⁴. RNaseH1(D145N) was rapidly recruited to UVC microbeam-irradiated sites in a transcription-dependent but ATM-independent manner (Fig. 5b and Extended Data Fig. 9d), suggesting R-loop formation at DNA-damage sites. The ability of RNaseH1(D145N) to detect R-loops was confirmed



by overexpression of active RNaseH1 or by silencing of RNaseH2, which prevented or potentiated, respectively, recruitment of RNaseH1(D145N) at UVC microbeam-irradiation sites (Extended Data Fig. 9a). Formation of R-loops at these sites was verified using the S9.6 DNA-RNA-hybrid-specific antibody³⁵ (Extended Data Fig. 9b). Silencing of RNaseH augments R-loop abundance and resulted in detectable immunofluorescence signals at nuclear areas irradiated with doses that normally do not elicit a detectable signal, thereby confirming the S9.6 antibody specificity (Extended Data Fig. 9c).

Overexpression of active RNaseH1 attenuated the UV-induced spliceosome mobilization to levels identical to ATM inhibition (Fig. 5c and Extended Data Fig. 9e). No additional effect was observed when the two manipulations were combined (Fig. 5c), suggesting that RNaseH1 mitigates the UV-triggered spliceosome mobilization by preventing ATM activation. Conversely, silencing of RNaseH1 and H2A, which resolve the majority of RNA-DNA duplexes within the cell^{30,36}, results in ATM activation (Extended Data Fig. 8a, b) and augments the UV-triggered R-loop formation (Extended Data Fig. 9c), spliceosome mobilization (Fig. 5d and Extended Data Fig. 9f, g) and intron retention (Fig. 5h).

ATM is required for a substantial fraction of the UV-triggered spliceosome mobilization. Regardless, ATM activation alone (for

example, as a result of ionizing radiation) does not influence spliceosome mobility (Figs 3a, 5e and Extended Data Fig. 5b), indicating that ATM controls a positive feedback mechanism that enhances, but cannot trigger, spliceosome displacement (Fig. 5i). We hypothesized that UV-dependent transcription inhibition acts as the initiating mechanism for spliceosome mobilization, which is then enhanced by a secondary ATM-dependent signal. To test this, we used treatments (DRB and ionizing radiation) that each can specifically influence one process; DRB inhibits transcription (Fig. 4a) but does not activate ATM (Extended Data Fig. 7a), while ionizing radiation activates ATM (Extended Data Figs 7a, e and 8d, e) but does not interfere with global transcription (Extended Data Fig. 5a). Combination of DRB and ionizing radiation had additive effects in both spliceosome mobilization and intron retention (Fig. 5e, g and Extended Data Fig. 10a, b), indicating that ATM amplifies (but does not initiate) a mobilization signal imposed by transcriptional arrest. In agreement, treatment of quiescent HDFs with CPT, which promotes formation of transcription-blocking lesions (Extended Data Fig. 10d) and R-loop-dependent ATM activation²⁸ (Extended Data Fig. 7e), can also efficiently mobilize spliceosomes to levels higher than expected by transcription inhibition alone (Fig. 5f and Extended Data Fig. 10c).

Discussion

Here we present evidence that the core spliceosome is a target and an effector of the cellular response to transcription-blocking DNA damage, and we define a previously uncharacterized ATM-dependent branch of genome surveillance. Transcription-blocking DNA lesions cause selective chromatin displacement of late-stage spliceosomes by a two-step mechanism involving a stochastic (*cis*) and an ATM-signalling-mediated (*trans*) stage. Our hypothesis is that displacement of assembled co-transcriptional spliceosomes is required to remove steric inhibition that would otherwise prevent back-tracking (or removal) of RNAPII from DNA lesions, which is critical for subsequent DNA repair²¹. The initial spliceosome displacement probably results in naked (intron-retaining) pre-mRNA readily available for hybridization with template single-strand DNA at the transcription bubble. This culminates in R-loop formation at damaged DNA sites, which in turn activate ATM. Previously, R-loop mediated ATM activation has been linked to replication-induced DSBs because of collision of arrested transcription complexes with the replication machinery^{30,37}. Here, we demonstrate that neither DSBs nor replication are required for R-loop-dependent ATM activation. While the exact mode of UV-triggered ATM activation remains to be determined, it does have significant biological consequences. It influences gene expression and plays a fundamental role in augmenting spliceosome displacement and alternative pre-mRNA splicing genome-wide.

ATM activation and spliceosome displacement are subject to reciprocal regulation, which has two unanticipated implications. First, in response to transcription-blocking lesions, changes in spliceosome organization activate ATM signalling irrespective of replication. Second, ATM modulates DDR, not only by controlling expression levels of its target genes, but also by influencing pre-mRNA processing. These observations provide new insights into the mechanisms and consequences of ATM activation in post-mitotic tissues, which is critical for proper cellular function, as evidenced by the severe neurodegeneration in ataxia telangiectasia patients³⁸.

Online Content Methods, along with any additional Extended Data display items and Source Data, are available in the online version of the paper; references unique to these sections appear only in the online paper.

Received 14 April 2014; accepted 11 May 2015.

Published online 24 June 2015.

1. Sirbu, B. M. & Cortez, D. DNA damage response: three levels of DNA repair regulation. *Cold Spring Harb. Perspect. Biol.* **5**, a012724 (2013).
2. Ciccia, A. & Elledge, S. J. The DNA damage response: making it safe to play with knives. *Mol. Cell* **40**, 179–204 (2010).

3. Hoeijmakers, J. H. DNA damage, aging, and cancer. *N. Engl. J. Med.* **361**, 1475–1485 (2009).
4. Shiloh, Y. & Ziv, Y. The ATM protein kinase: regulating the cellular response to genotoxic stress, and more. *Nature Rev. Mol. Cell Biol.* **14**, 197–210 (2013).
5. Kaidi, A. & Jackson, S. P. KAT5 tyrosine phosphorylation couples chromatin sensing to ATM signalling. *Nature* **498**, 70–74 (2013).
6. Lenzken, S. C., Loffreda, A. & Barabino, S. M. RNA splicing: a new player in the DNA damage response. *Int. J. Cell Biol.* **2013**, 153634 (2013).
7. Hoskins, A. A. & Moore, M. J. The spliceosome: a flexible, reversible macromolecular machine. *Trends Biochem. Sci.* **37**, 179–188 (2012).
8. Valadkhan, S. & Jaladat, Y. The spliceosomal proteome: at the heart of the largest cellular ribonucleoprotein machine. *Proteomics* **10**, 4128–4141 (2010).
9. Kornblihtt, A. R. *et al.* Alternative splicing: a pivotal step between eukaryotic transcription and translation. *Nature Rev. Mol. Cell Biol.* **14**, 153–165 (2013).
10. Schor, I. E., Gomez Acuna, L. I. & Kornblihtt, A. R. Coupling between transcription and alternative splicing. *Cancer Treat. Res.* **158**, 1–24 (2013).
11. Zhou, H. L., Luo, G., Wise, J. A. & Lou, H. Regulation of alternative splicing by local histone modifications: potential roles for RNA-guided mechanisms. *Nucleic Acids Res.* **42**, 701–713 (2014).
12. Alexander, R. & Beggs, J. D. Cross-talk in transcription, splicing and chromatin: who makes the first call? *Biochem. Soc. Trans.* **38**, 1251–1256 (2010).
13. Dutertre, M., Sanchez, G., Barbier, J., Corcos, L. & Auboeuf, D. The emerging role of pre-messenger RNA splicing in stress responses: sending alternative messages and silent messengers. *RNA Biol.* **8**, 740–747 (2011).
14. Paronetto, M. P., Minana, B. & Valcarcel, J. The Ewing sarcoma protein regulates DNA damage-induced alternative splicing. *Mol. Cell* **43**, 353–368 (2011).
15. Dutertre, M. *et al.* Cotranscriptional exon skipping in the genotoxic stress response. *Nature Struct. Mol. Biol.* **17**, 1358–1366 (2010).
16. Muñoz, M. J. *et al.* DNA damage regulates alternative splicing through inhibition of RNA polymerase II elongation. *Cell* **137**, 708–720 (2009).
17. Cox, J. & Mann, M. MaxQuant enables high peptide identification rates, individualized p.p.b.-range mass accuracies and proteome-wide protein quantification. *Nature Biotechnol.* **26**, 1367–1372 (2008).
18. Rino, J. *et al.* A stochastic view of spliceosome assembly and recycling in the nucleus. *PLoS Comput. Biol.* **3**, 2019–2031 (2007).
19. Dinant, C. *et al.* Activation of multiple DNA repair pathways by sub-nuclear damage induction methods. *J. Cell Sci.* **120**, 2731–2740 (2007).
20. Lagerwerf, S., Vrouwe, M. G., Overmeer, R. M., Fouteri, M. I. & Mullenders, L. H. DNA damage response and transcription. *DNA Repair (Amst.)* **10**, 743–750 (2011).
21. Vermeulen, W. & Fouteri, M. Mammalian transcription-coupled excision repair. *Cold Spring Harb. Perspect. Biol.* **5**, a012625 (2013).
22. Matsuoka, S. *et al.* ATM and ATR substrate analysis reveals extensive protein networks responsive to DNA damage. *Science* **316**, 1160–1166 (2007).
23. Blasius, M. *et al.* A phospho-proteomic screen identifies substrates of the checkpoint kinase Chk1. *Genome Biol.* **12**, R78 (2011).
24. Ahn, E. Y. *et al.* SON controls cell-cycle progression by coordinated regulation of RNA splicing. *Mol. Cell* **42**, 185–198 (2011).
25. Lee, J. H. & Paull, T. T. ATM activation by DNA double-strand breaks through the Mre11-Rad50-Nbs1 complex. *Science* **308**, 551–554 (2005).
26. Bakkenist, C. J. & Kastan, M. B. DNA damage activates ATM through intermolecular autophosphorylation and dimer dissociation. *Nature* **421**, 499–506 (2003).
27. Matsuoka, S., Huang, M. & Elledge, S. J. Linkage of ATM to cell cycle regulation by the Chk2 protein kinase. *Science* **282**, 1893–1897 (1998).
28. Sordet, O. *et al.* Ataxia telangiectasia mutated activation by transcription- and topoisomerase I-induced DNA double-strand breaks. *EMBO Rep.* **10**, 887–893 (2009).
29. Hanasoge, S. & Ljungman, M. H2AX phosphorylation after UV irradiation is triggered by DNA repair intermediates and is mediated by the ATR kinase. *Carcinogenesis* **28**, 2298–2304 (2007).
30. Aguilera, A. & Garcia-Muse, T. R loops: from transcription byproducts to threats to genome stability. *Mol. Cell* **46**, 115–124 (2012).
31. Huertás, P. & Aguilera, A. Cotranscriptionally formed DNA:RNA hybrids mediate transcription elongation impairment and transcription-associated recombination. *Mol. Cell* **12**, 711–721 (2003).
32. Kotake, Y. *et al.* Splicing factor SF3b as a target of the antitumor natural product pladienolide. *Nature Chem. Biol.* **3**, 570–575 (2007).
33. Cerritelli, S. M. & Crouch, R. J. Ribonuclease H: the enzymes in eukaryotes. *FEBS J.* **276**, 1494–1505 (2009).
34. Wu, H., Lima, W. F. & Crooke, S. T. Investigating the structure of human RNase H1 by site-directed mutagenesis. *J. Biol. Chem.* **276**, 23547–23553 (2001).
35. Bhatia, V. *et al.* BRCA2 prevents R-loop accumulation and associates with TREX-2 mRNA export factor PCID2. *Nature* **511**, 362–365 (2014).
36. Reijns, M. A. M. *et al.* Enzymatic Removal of Ribonucleotides from DNA Is Essential for Mammalian Genome Integrity and Development. *Cell* **149**, 1008–1022 (2012).
37. McManus, C. J. & Graveley, B. R. RNA structure and the mechanisms of alternative splicing. *Curr. Opin. Genet. Dev.* **21**, 373–379 (2011).
38. Biton, S., Barzilai, A. & Shiloh, Y. The neurological phenotype of ataxia-telangiectasia: solving a persistent puzzle. *DNA Repair (Amst.)* **7**, 1028–1038 (2008).

Supplementary Information is available in the online version of the paper.

Acknowledgements We acknowledge the Optical Imaging Center of ErasmusMC for technical support; M. Reijns and A. Jackson for the S9.6 antibody; L. Marufu for technical assistance; and N. G. J. Jaspers for intellectual input. This work was funded by the Netherlands Organization for Scientific Research (NWO) ZonMW TOP Grants 912.08.031 and 912.12.132, Horizon Zenith 935.11.042, ALW 854.11.002 and 823.02.013, the Association for International Cancer Research 10-594, European Research Council Advanced Investigator Grants 233424 and 340988, and an ErasmusMC fellowship.

Author Contributions M.T. designed the study, performed the majority of experiments, analysed the data and authored the manuscript with contributions from W.V. and J.A.M. J.A.A.D. performed the liquid-chromatography tandem mass spectrometry analysis, L.S. assisted in fractionation/immunoblotting experiments, J.A.M. performed S9.6 antibody immunofluorescence and assisted in UVC micro-irradiation experiments, D.W. and R.H.M. performed RT-PCR splicing assays, P.K., F.G.G. and W.v.I.J. performed RNA-seq experiments, L.H.M. and M.G.V. generated RNaseH1 constructs and cell lines. L.H.M. and J.H.J.H. provided advice. All authors reviewed and commended on the manuscript.

Author Information RNA-seq data have been deposited in the Sequence Read Archive with accession number SRP053034. Reprints and permissions information is available at www.nature.com/reprints. The authors declare no competing financial interests. Readers are welcome to comment on the online version of the paper. Correspondence and requests for materials should be addressed to M.T. (m.tresini@erasmusmc.nl), W.V. (w.vermeulen@erasmusmc.nl) or J.A.M. (j.marteijn@erasmusmc.nl).

METHODS

Materials. Micrococcal nuclease (MNase) and all chemicals were purchased from Sigma-Aldrich unless otherwise specified. DNA-modifying enzymes were from Roche Applied Sciences. Pladienolide B was from Santa Cruz Biotechnology, the ATR inhibitor VE821 from TINIB-Tools, and the ATM inhibitor KU55933 and DNA-PK inhibitor NU7441 from R&D Systems. Antibodies used were against: PRP8 (H300), XPA/p62 (FL-273), p89/XPB (S-19) and β -tubulin from Santa Cruz Biotechnology; SNRPC/U1C (NBP1-96048), NHP2L1 (NBP1-32732), SF3a1 (NB100-79847), SF3b2 (NV100-79843), RNaseH1 (NBP2-20171), and RNaseH2A (NBP1-76981) from Novus Biologicals; SNRNP40 (SAB2701506) and SRSF2/SC35 (clone SC-35) from Sigma; SNRPA/U1A (3F9-1F7) from ABGENT; PRPF3 (ab187535), RNPII CTD (phospho-S2) (ab5095), RNAPII (ab5095), PCNA (PC-10), Ki67 (ab833) from abcam; CPD (TDM-2) from MBL International; GFP (11 814 460 001) from Roche; H2A (07-146) from Millipore Corp.; phospho-ATM(1981)(05-740) from Upstate Biotechnology, phospho-CHK2(Thr68) (2661) from Cell Signaling. Anti-XPC (rabbit-polyclonal ab) was in-house developed. Odyssey-compatible IRDye680- and IRDye800-conjugated secondary antibodies were from LI-COR. Secondary antibodies conjugated to Alexa Fluorochromes-488, -568, -594 and -647 were from Invitrogen. GFP-tagged proteins were immunoprecipitated with GFP-Trap beads (ChromoTek).

Cell culture, SILAC labelling and cell treatments. Cell lines used in this study were: ataxia telangiectasia patient (AT2)- and healthy adult donor (C5Ro)-derived human dermal fibroblasts (HDFs); SV40-transformed XPA (XP12RO), XPC (XP4A) and CSB (CS1AN) patient-derived HDFs; hTERT immortalized HDFs (C5Ro-T), VH10 human foreskin fibroblasts (VH10-T) and human retinal pigmented epithelial cells (RPE1, ATCC), human osteosarcoma cells (U2OS, ATCC); and the amphotropic retroviral packaging cell line Gryphon A (Allele Biotechnology). Cells were subcultured under standard culture conditions (37 °C, 5% CO₂) in a humidified incubator. U2OS, Gryphon A, and SV40-transformed cells were grown in Dulbecco's Modified Eagle's Medium (DMEM, Lonza), supplemented with 10% v/v fetal bovine serum (FBS, Fisher Scientific) and 1% v/v penicillin-streptomycin (PS, Lonza). Primary and TERT-immortalized HDFs and RPE-1 cells were cultured in Ham's F10 (Lonza) supplemented with 15% FBS and 1% PS. When applicable, cells were synchronized in quiescence by 72 h serum-deprivation. For FRAP and immunofluorescence experiments, cells were seeded on 25-mm-diameter glass slides. For UVC laser/live-cell-imaging experiments, cells were seeded on quartz coverslips (010191T-AB; SPI Supplies). For stable isotopic labelling with amino-acids in culture (SILAC), C5Ro-T cells were cultured for >5 population doublings (PD) in lysine-, arginine- and leucine-free DMEM (AthenaES) supplemented with antibiotics, non-essential amino-acids (Lonza), 10% dialysed FBS (Invitrogen) and 105 $\mu\text{g ml}^{-1}$ leucine and either 73 $\mu\text{g ml}^{-1}$ light [¹²C₆]lysine and 42 $\mu\text{g ml}^{-1}$ [¹²C₆, ¹⁴N₄]arginine or with heavy [¹³C₆]lysine and [¹³C₆, ¹⁵N₄]arginine (Cambridge Isotope Laboratories). In each subcultivation, cell numbers were determined using a Beckman Z2 coulter counter (Beckman Coulter, Inc.), and 0.5 $\times 10^4$ cells were seeded per cm² of growth surface area. The increase in population doubling (ΔPD) was calculated using the formula $\Delta\text{PD} = \log_{10}(\text{number of cells harvested}/\text{number of cells seeded})/\log_{10}(2)$.

Cells were UVC irradiated (254 nm, TUV Lamp, Philips) at the indicated doses. For local DNA damage infliction, cells were UV-irradiated (60 J m⁻²) through isopore polycarbonate membranes containing 5- μm -diameter pores (Millipore). Chemicals were added directly in the growth media at the indicated concentrations. In FRAP experiments cells were assayed 1 h after initiation of treatment with the exception of illudrin S and rotenone, which were assayed at 6 h. Pre-incubation with caffeine (10 mM), DDR-kinase inhibitors (10 μM) and MG132 (50 μM), started 1 h before genotoxic treatments and lasted throughout the experiment. α -Amanitin treatments were for >24 h. For exon-specific RT-PCR cells were lysed 6 h after treatment.

Mass spectrometry and data analysis. Nanoflow liquid chromatography-tandem mass spectrometry (LC-MS/MS) and data analysis were as described³⁹. In brief, samples containing MNase-digested chromatin were size-fractionated by SDS-PAGE, gels were cut in 2-mm slices, and subjected to dithiothreitol-reduction, iodoacetamide alkylation and trypsin digestion. LC-MS/MS was performed on an 1100 series capillary liquid chromatography system (Agilent Technologies) coupled to an LTQ-Orbitrap XL mass spectrometer (Thermo Scientific) operating in positive mode. Raw mass spectrometry data were analysed using the MaxQuant software. A false discovery rate of 0.01 for proteins and peptides and a minimum peptide length of six amino acids were set. The Andromeda search engine was used to search MS/MS spectra against the International Protein Index (IPI) human database. Statistical analysis was performed with Perseus (1.5.0.30)¹⁷.

Cloning. Human full-length cDNA clones used for subcloning were; PRP8/PRPF8/DHX16 (CS116070), SF3A1 (SC321295), SNRPN40 (SC112670) and RNaseH1 (SC319446) from Origene and U1A/SNRPA (MHS6278-202826119), NHP2L1 (MHS6278-202839330) and PRP3/PRPF3 (MHS6278-202826220) from Dharmacon. To generate vectors expressing GFP- and mCherry-tagged proteins the open reading frames (minus the stop codon) of human U1A, SF3a1, PRP3, NHP2L1, PRP8 and SNRNP40 were PCR amplified using oligonucleotides containing restriction enzyme sites. PCR products were subcloned into a pLHCX retroviral expression vector (Clontech Laboratories) modified to contain eGFP lacking the initiation codon. XPA and RNaseH1 lacking the mitochondrial localization signal (amino acids 1–28) were subcloned in modified pLHCX vectors containing either eGFP or mCherry lacking their stop codons. PCR amplifications were performed on a MJ Scientific, Inc., PTC-100 Thermocycler using high-fidelity Phusion polymerase (Bioke). Amplified cDNAs were purified using the Promega Wizard kit. Following restriction digestion of inserts and vectors, shrimp alkaline phosphatase treatment of the vectors, and agarose gel electrophoresis, the gel-excised DNAs were purified using the Promega Wizard kit. DNA inserts were ligated into vectors at a 3:1 molar ratio. Plasmid DNAs were validated by restriction digestion and sequencing.

Infections/transfections. C5Ro-T, C5Ro, AT-2, U2OS and VH-10T cell lines stably expressing GFP-tagged proteins were generated by retroviral infection followed by hygromycin selection. For retrovirus production Gryphon A cells were transfected with the appropriate expression vector using FuGENE 6 (Roche) according to the manufacturer's instructions. Viral supernatants were harvested 48 h post-transfection, filtered through 0.45- μm filters (Millipore Corp.) and used immediately to infect subconfluent cell cultures in the presence of 5 $\mu\text{g ml}^{-1}$ polybrene. U2OS cells were transiently transfected with RNaseH1-mCherry (pLHCX) using FuGENE 6. For gene silencing the following siRNAs were purchased from Thermo Scientific as SMARTpools: ON-TARGETplus Human RNaseH2A siRNA (L-003535-01-0005) targeting the catalytic subunit A of RNaseH2, ON-TARGETplus RNaseH1 siRNA (L-012595-01-0005), ON-TARGETplus PRP8 siRNA (L-012252-01-0005), ON-TARGETplus SF3a1 siRNA (L-016051-01-0005), ON-TARGETplus ATM siRNA (L-003201-00-00005) and a control/scrambled siRNA duplex (D-001210-05-05). For gene silencing, U2OS cells were transfected with RNAiMAX (Invitrogen), and C5RoT and RPE cells with HiPerfect (Qiagen), as recommended by the manufacturers. To inhibit endogenous RNaseH activity cells were transfected with a (1:1) mixture of siRNAs targeting RNaseH1 and RNaseH2A.

Preparation of whole cell lysates, chromatin fractionation, and immunoprecipitations. Whole-cell lysates were prepared by lysis of equal cell numbers in 60 mM Tris-Cl (pH 6.8), 2% SDS, 10% glycerol, 5% β -mercaptoethanol and 0.01% bromophenol blue. Crude chromatin was isolated after Triton-X 100 extraction and MNase digestion. All fractionation steps were performed at 4 °C. Cell pellets were suspended in a non-denaturing isosmotic buffer (10 mM PIPES (pH 7.0), 3 mM MgCl₂, 100 mM NaCl, 300 mM sucrose, 0.5 mM Na₂VO₄, 5 mM NaF, 5 mM Na₄P₂O₇, 10 mM β -glycerolphosphate, 0.1 mM PMSF, 1 mM EGTA, 1 \times EDTA-free protease inhibitor cocktail (Roche), 15 μM MG132, 10 mM N-ethylmaleimide and 20 μM PR-619 (LifeSensors)) and extracted in the same buffer with 0.5% (v/v) Triton-X 100 for 5 min. Following centrifugation (650g, 5 min), nuclei depleted from soluble nucleoplasm were washed with MNase digestion buffer (50 mM Tris-Cl (pH 7.5), 4 mM MgCl₂, 50 mM KCl, 300 mM sucrose, 0.5 mM Na₂VO₄, 5 mM NaF, 5 mM Na₄P₂O₇, 10 mM β -glycerolphosphate, 1 mM PMSF, 1 mM EGTA and 1 \times EDTA-free protease inhibitor cocktail) and subsequently incubated with 0.3 U MNase (Sigma)/1 $\times 10^6$ nuclei, and 1 mM CaCl₂ (37 °C, 10 min). Addition of (NH₄)₂SO₄ to a final concentration of 250 mM was used to facilitate extraction of stably DNA-bound proteins. EGTA and EDTA were added to 5 mM and samples were centrifuged at 16,000g for 20 min. Protein concentrations were determined using a modified Bradford method (Bio-Rad). For GFP immunoprecipitations, cells were lysed in 20 mM Tris-Cl (pH 7.5), 5 mM MgCl₂, 150 mM NaCl, 0.5% Triton X-100, 1 \times phosphatase inhibitor (Roche) and 1 \times protease inhibitor cocktail. Chromatin was mechanically sheared by passing through a 27G syringe, 40 times. Particulate matter was removed by centrifugation (20 min at 16,000g) and supernatants containing equal amounts of proteins were used for immunoprecipitation. GFP-tagged proteins were immunoprecipitated directly or after MNase digestion which was used to cleave DNA and RNA and disrupt ternary complexes. Samples were incubated (2 h, 4 °C) with pre-equilibrated GFP-Trap coupled to agarose beads (ChromoTek), and after extensive washing (10 mM Tris-Cl (pH 7.5), 150 mM NaCl, 0.5 mM EDTA, 0.5% NP-40), immunocomplexes were dissociated from the beads by heating for 10 min at 95 °C, in 120 mM Tris-Cl (pH 6.8), 4% SDS, 20% glycerol, 10% β -mercaptoethanol, 0.01% bromophenol blue. For immunoprecipitation of elongating RNAPII, cells were treated and extracted as for isolation of crude chromatin with the exception that instead of MNase

digestion, chromatin was mechanically sheared. Immunoprecipitations were performed by O/N incubation with either the anti-RNAPII CTD phospho-Ser2 antibody or rabbit IgG, followed by incubation with protein A/protein G agarose beads (Upstate Biotechnology).

Immunoblotting. Protein samples were size-fractionated on 5–20% gradient SDS-polyacrylamide gels (BioRad) and electro-transferred onto nitrocellulose membranes using a Bio-Rad Mini-Protean electrophoresis system. Abundance of proteins of interest was assayed using antibodies at concentrations recommended by their manufacturers. Membranes were incubated with primary antibodies in Tween 20/Tris-buffered saline (20 mM Tris (pH 7.4), 150 mM NaCl, 0.1% Tween 20) containing 3% w/v non-fat dry milk or, when the pATM antibody was used, 3% BSA. Following binding of the appropriate anti-mouse or anti-rabbit Alexa Fluorochrome-conjugated secondary antibody and extensive washing, proteins of interest were visualized using the Odyssey CLx Infrared Imaging System (LI-COR Biosciences). Signal intensities were quantified using the ImageQuant TL software (GE Healthcare Life Sciences).

RNA synthesis. Transcription levels were determined following 2-hour incubation with ethynyluridine (EU)⁴⁰ added directly in the culture (serum-free) media. EU incorporation was visualized using Click-iT conjugation of AlexaFluor647 (Invitrogen) according to the manufacturer's protocol. Images were obtained using a Zeiss Axio Imager Z2 upright laser-scanning confocal microscope equipped with a 63× Plan-Apochromat 1.4 NA oil-immersion lens (Carl Zeiss Inc.). Fluorescence-signal intensities were quantified using the ImageJ software (NIH). In each experiment >150 cells per condition were analysed.

Immunofluorescence and live-cell confocal laser-scanning microscopy. For immunofluorescence experiments, cells were fixed with 3.7% paraformaldehyde (PFA)/PBS and permeabilized in 0.5% Triton-X 100/PBS. For detection of splicing factors and XPC, cells were pre-extracted with 0.5% Triton-X 100/PBS before fixation (0.5 min). For CPD immunodetection, nuclear DNA was denatured with 0.07 M NaOH for 5 min. For SRSF2/SC35 immunodetection cells fixed in 2% PFA/0.2% Triton-X 100/PBS were treated with 100% acetone (5 min, –20 °C). Non-specific antigens were blocked in 3% BSA/PBS. R-loop immunodetection with the S9.6 antibody was as described previously³⁵. In brief, PFA-fixed cells were permeabilized by Triton X-100, followed by extraction with 0.5% SDS. Cells were blocked with 3% BSA, 0.1% Tween 20 in 4 × Saline Sodium Citrate (SSC) buffer. Hybridization of primary antibodies was overnight at 4 °C, and with secondary Alexa Fluorochrome-conjugated antibodies for 1 h at room temperature. Coverslips were mounted on glass slides using 4,6-diamidino-2-phenylindole (DAPI)-containing ProLong Gold antifade reagent (Molecular probes) and imaged on a Zeiss Axio Imager Z2 upright laser-scanning confocal microscope.

Live-cell-imaging experiments were performed with a Leica TCS SP5 AOBs laser scanning confocal microscope equipped with an environmental chamber (37 °C, 5% CO₂). Kinetic studies of GFP-tagged proteins were performed using UVC (266 nm)-laser-irradiation for local DNA damage infliction¹⁹. In brief, a 2 mW pulsed (7.8 kHz) diode-pumped solid-state laser emitting at 266 nm (Rapp OptoElectronic) was connected to the confocal microscope with an Axiovert 200M housing adapted for UV by all-quartz optics. By focusing the UVC laser inside cell nuclei without scanning, only a limited area within the nucleus (diffraction limited spot) was irradiated. Cells were imaged and irradiated through a 100×, 1.2 NA Ultrafluor quartz objective lens. Images obtained before and after UVC laser irradiation were analysed using the LASAF software (Leica). Fluorescence intensity in the irradiated area or a non-irradiated area in the nucleus was normalized to levels in the same area before irradiation. Data were expressed as the percentage change in relative fluorescence intensity. In each experiment at least ten cells were analysed and all experiments were performed a minimum of three times.

Mobility of GFP-tagged proteins was measured by strip-FRAP as described⁴¹. In brief, a narrow (~1 μm) strip spanning the width of the nucleus was photobleached at ~20% of the initial GFP-signal intensity using a 488 nm laser at 100% power. Recovery of fluorescence in the strip was monitored at 25-ms intervals. Images obtained were analysed using the LASAF software (Leica). FRAP data were normalized to the fluorescence levels before photobleaching after subtraction of the background signal. In each experiment 8–10 cells per condition were analysed and all experiments were performed at least three times. A negative (untreated) and positive (20 J cm⁻² UV) control were included in all experiments.

Chromatin-associated RNA isolation and snRNA qPCR. Chromatin-associated RNA was isolated by a modification of the method developed by Wu and Schibler⁴² for the isolation of ternary-complex-associated nascent RNA. Briefly, cell pellets were re-suspended in 20 mM HEPES (pH 7.5), 10 mM KCl, 250 mM sucrose, 5 mM MgCl₂, 1 mM EGTA, 1 mM PMSF, 1 μl ml⁻¹ RNasin (Invitrogen), 1× phosphatase inhibitor (PhosStop, Roche) and 1× protease inhibitor cocktail (Roche), and lysed by the addition of Digitonin

to 200 μg ml⁻¹ final concentration (10 min, 4 °C). Nuclei were pelleted by centrifugation (650g, 5 min) and following re-suspension in a buffer containing 20 mM Tris-HCl (pH 7.5), 75 mM NaCl, 0.5 mM EGTA, 50% glycerol, 1 mM PMSF, 1 μl ml⁻¹ RNasin, 1× protease and 1× phosphatase inhibitors, were extracted for 10 min at 4 °C by the addition of ten volumes of a solution containing 20 mM HEPES (pH 7.6), 7.5 mM MgCl₂, 0.2 mM EGTA, 300 mM NaCl, 1 M urea and 1% NP-40. Pelleted nuclei were re-suspended in Qiazol reagent (Qiagen) and RNA was isolated as recommended by the manufacturer. Following digestion with DNase I (Qiagen) RNA was cleaned up with the Qiagen RNeasy mini-kit with a second, on-column, DNase I digestion. Equal amounts of RNA from each sample were reverse-transcribed using random-hexamers and SuperScript III (Invitrogen). qPCR reactions were performed using primers complementary to human snRNAs (described and validated by Galiveti *et al.*⁴³) or the chromatin-associated HotAir ncRNA (control for data normalization), using the IQSYBR Green Supermix (Bio-Rad) in a CFX96 Touch Real-Time PCR Detection System (Bio-Rad). Absence of contaminating genomic DNA was verified by the lack of amplified products for all sample/primer sets by inclusion of mock reverse-transcription reactions in which no enzyme was added.

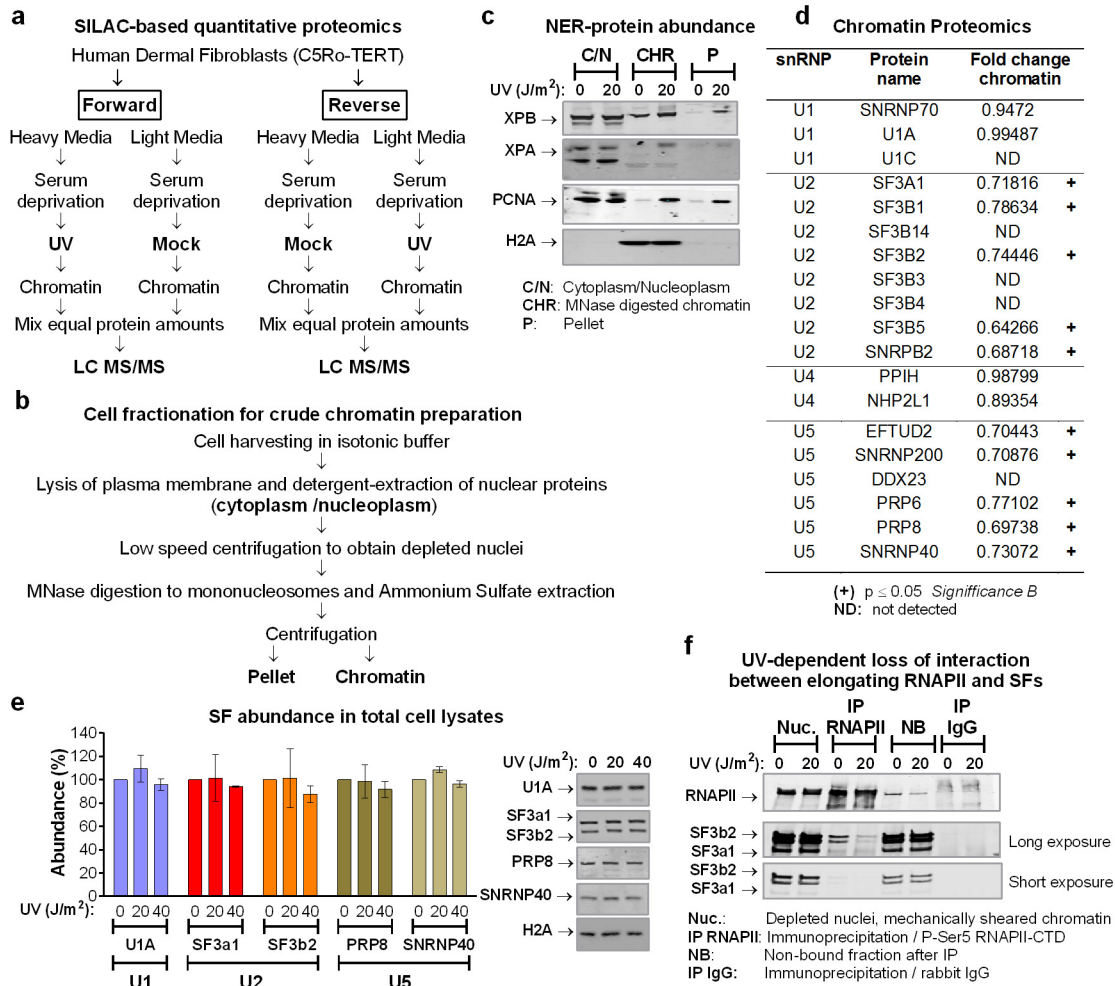
Exon-specific RT-PCR: RNA extraction, reverse transcription and PCR. Experiments were performed as described by Ahn *et al.*²⁴. In brief, RNA was isolated from quiescent RPE-1 cells using the RNeasy kit (QIAGEN). Equal RNA amounts from each sample were reverse transcribed using random hexamers and SuperScript III RT and cDNAs were PCR-amplified using the indicated primers and Taq DNA Polymerase (NEB). PCR products were size-fractionated by gel electrophoresis and visualized by ethidium bromide staining. Signal intensities of amplified fragments containing either the unspliced or the spliced intron were normalized to the levels of the respective fragments in untreated cells and expressed as fold change in relative abundance. All experiments were repeated a minimum of three times. Amplification of constitutive exons from TUBA1B and GAPDH were used as controls for general splicing efficiency. Primers sets used for amplifications were: FANCG (exon5–6) 5'-GGATGTCTCCTGACAGC AT-3' and 5'-GCTGTGTACACCTGGACCAA-3'; AKT1 (exon11–12) 5'-AC AAGACGGGCACATTAAG-3' and 5'-ACCGACATCATCTCGTACA-3'; AURKA (exon9–10) 5'-AATGATTGAAGTCCGGATGC-3' and 5'-TCTGGC TGGGATTATGCTTC-3'; AURKB (exon6–7) 5'-TGCAGAAGAGCTGCACAT TT-3' and 5'-TCTCAGCTCTCCCTTGAGC-3'; TUBA1B (exon2–3) 5'-CC GGGCTGTGTTGTAGACT-3' and 5'-GATCTCCTTGCCAATGGTGT-3'; ATM (exon19–20) 5'-AAGGAGCTTCTGGAGAAGAG-3' and 5'-AACT GCTCTAGACATCCCTT-3'; ATR (exon33–34) 5'-AAGAGCCATATCCT GGCTCTC-3' and 5'-CTACCCTGGCACTCTGCAGCC-3'.

Paired-end RNA-seq and data analysis. RPE-1 cells were grown to confluence and serum-deprived for 72 h to ensure quiescence. Cells were then mock-treated or UV-irradiated with 20 J m⁻² UVC (245 nm), in the presence or absence of 10 μM of the ATM inhibitor. Each treatment was performed in duplicate plates that were used as biological replicates. RNA was isolated 6 h post-irradiation with the RNeasy kit (QIAGEN) and PolyA RNA was isolated using the Dynabeads mRNA purification kit (Invitrogen). Sample integrity was verified by the Agilent 2100 Bioanalyzer (Agilent Technologies). For all samples the Bioanalyzer RNA integrity scores (RIN) were 9.3–10, indicating excellent RNA quality. For each sample a cDNA library was prepared and validated using the Illumina TruSeq RNA sample preparation kit v2 according to the manufacturer's instructions. In brief, equal amounts (200 ng) of poly(A)-RNA were chemically fragmented, cDNA was generated using random hexamers as primers and adapters were ligated. RNA fragmentation efficiency and similarity between samples was confirmed by the Bioanalyzer after adaptor ligation (average fragment sizes were 317–344 bp). Following PCR amplification RNA-seq was performed according to the Illumina TruSeq v3 protocol on the HiSeq2500 platform, generating paired-end, 100-bp reads (9 × 10⁷ reads per sample). Raw reads were aligned against the human genome assembly (hg19) using TopHat⁴⁴. Uniquely mapped reads were used for the identification of alternative splicing events using multi-variate analysis of transcript splicing (MATS) as previously described⁴⁵. Alternative splicing events that were significantly increased ($P < 0.05$, $n = 2$) by UV irradiation (untreated versus UV-irradiated cells) by a minimum of 10% difference were considered to be UV-induced. Each individual alternative splicing event identified in the first analysis to be UV-induced that also decreased by a minimum of 10% in UV-irradiated cells in absence of ATM activity (UV-irradiated cells versus ATM-inhibitor-treated/UV-irradiated cells) was considered to be (partly) dependent on ATM activity.

Statistical analysis. All data presented were reproduced in at least three independent experiments. Statistical analysis was performed using the PRIZM GraphPad software unless otherwise stated. Significance of differences was evaluated with either Student's *t*-test, when only two groups were compared, or

one-way ANOVA for more than two groups. No statistical methods were used to predetermine sample size. One-way ANOVA was followed by post hoc analysis either by Dunnett's test (for comparison of experimental conditions to control) or Bonferroni's test (comparison between groups). * $P < 0.05$, ** $P < 0.01$ and *** $P < 0.001$. Proteomic data statistical analysis was performed with Perseus (1.5.0.30)¹⁷. Significance B was calculated by estimating the variance of the distribution of all protein ratios, taking into account the dependency of the distribution on the summed protein intensity¹⁷. Peptides with a significance B value $P \leq 0.05$ in either the forward or reverse experiment were considered significant and indicated by (+) in Extended Data Fig. 1d and Supplementary Table 1. Significant alternative splicing events were identified by MATS⁴⁵; only UV-triggered events with $P < 0.05$ were used for further analysis.

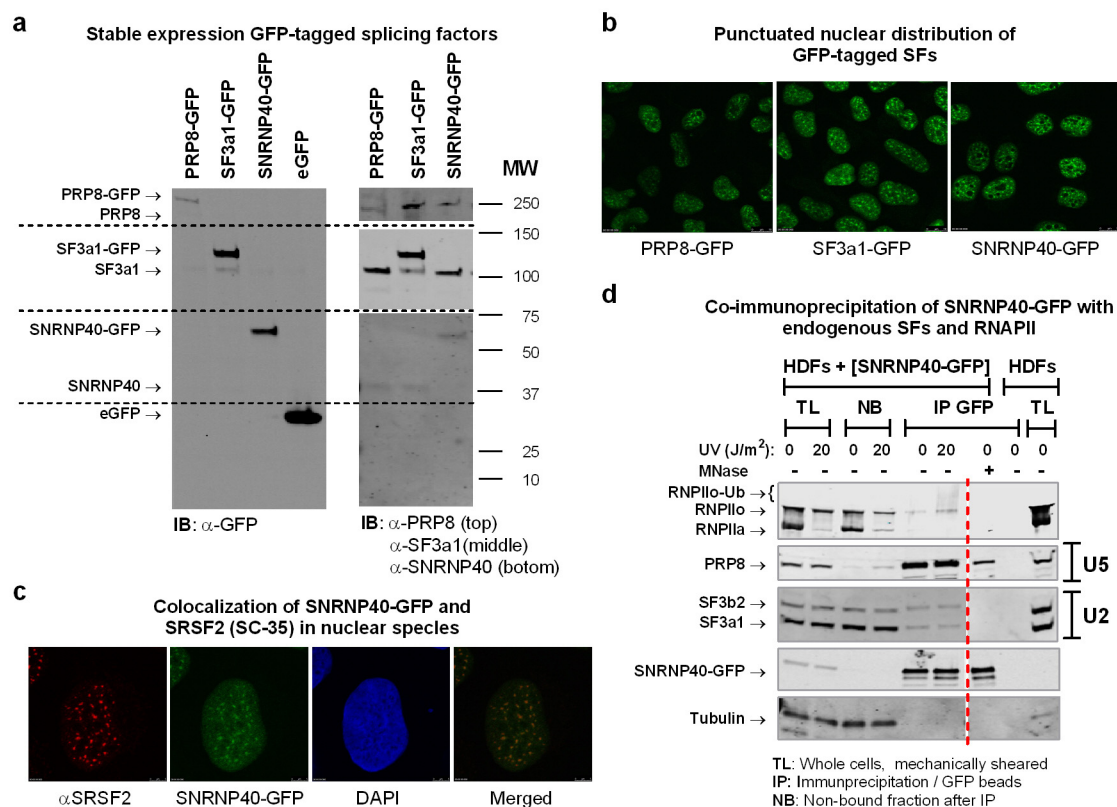
39. Schwertman, P. *et al.* UV-sensitive syndrome protein UVSSA recruits USP7 to regulate transcription-coupled repair. *Nature Genet.* **44**, 598–602 (2012).
40. Nakazawa, Y., Yamashita, S., Lehmann, A. R. & Ogi, T. A semi-automated non-radioactive system for measuring recovery of RNA synthesis and unscheduled DNA synthesis using ethynyluracil derivatives. *DNA Repair (Amst.)* **9**, 506–516 (2010).
41. Houtsmuller, A. B. & Vermeulen, W. Macromolecular dynamics in living cell nuclei revealed by fluorescence redistribution after photobleaching. *Histochem. Cell Biol.* **115**, 13–21 (2001).
42. Wuarin, J. & Schibler, U. Physical isolation of nascent RNA chains transcribed by RNA polymerase II: evidence for cotranscriptional splicing. *Mol. Cell. Biol.* **14**, 7219–7225 (1994).
43. Galiveti, C. R., Rozhdestvensky, T. S., Brosius, J., Lehrach, H. & Konthur, Z. Application of housekeeping npcRNAs for quantitative expression analysis of human transcriptome by real-time PCR. *RNA* **16**, 450–461 (2010).
44. Trapnell, C., Pachter, L. & Salzberg, S. L. TopHat: discovering splice junctions with RNA-Seq. *Bioinformatics* **25**, 1105–1111 (2009).
45. Shen, S. *et al.* MATS: a Bayesian framework for flexible detection of differential alternative splicing from RNA-Seq data. *Nucleic Acids Res.* **40**, e61 (2012).



Extended Data Figure 1 | Chromatin association of splicing factors.

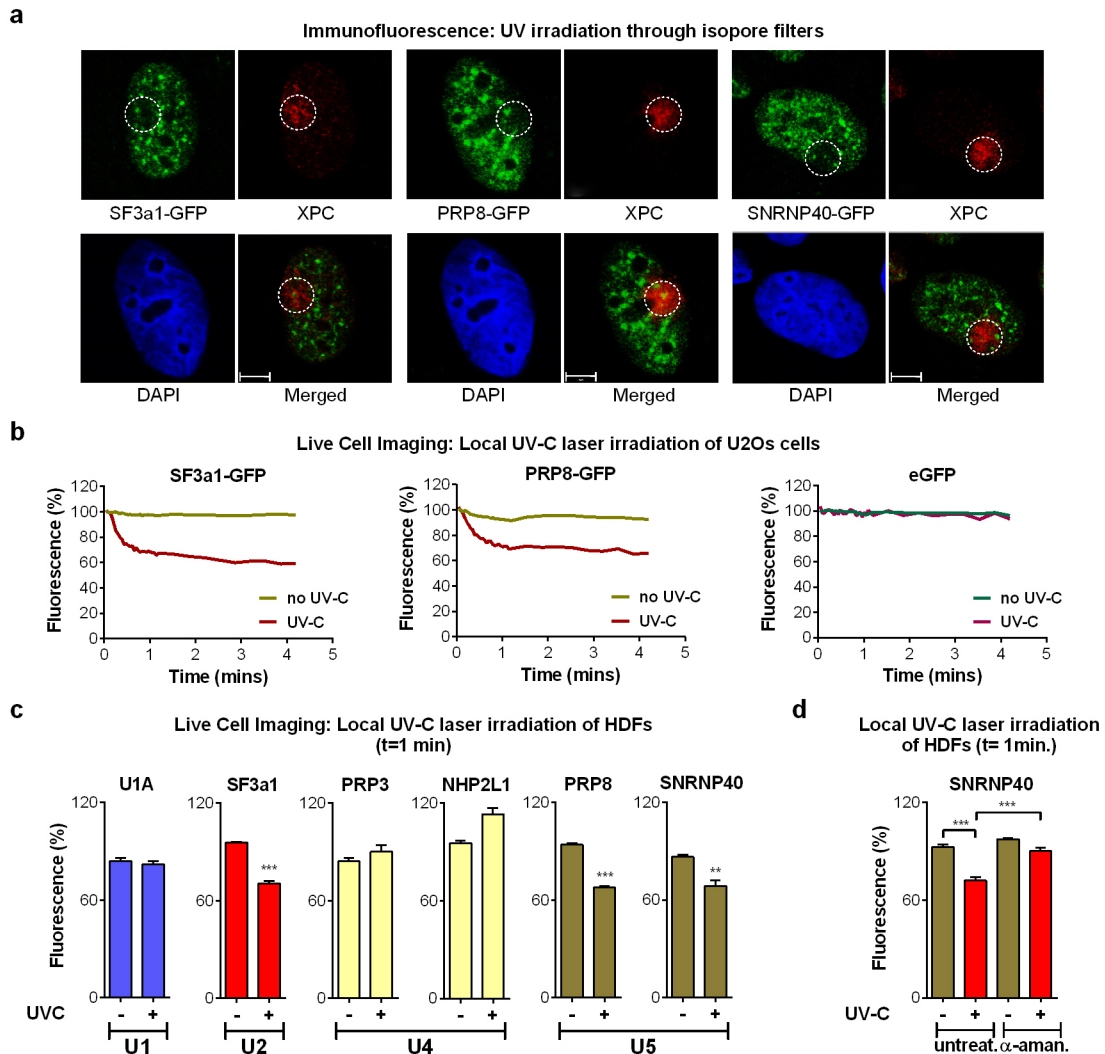
a, Schematic overview of the proteomic experiments for the identification of proteins that display UV-dependant chromatin association. **b**, Schematic outline of cell fractionation. **c**, Validation of the chromatin-isolation protocol for NER proteins that are recruited to chromatin in response to DNA damage. Mock-treated or UV-irradiated quiescent HDFs (20 J m^{-2} , 1 h post-irradiation) were fractionated as outlined in **b**. Equal protein amounts from each fraction were analysed by immunoblotting using antibodies against the indicated NER proteins. Abundance of H2A is shown as a control for chromatin-isolation efficiency. **d**, UV-triggered changes in chromatin association of core splicing factors, identified by quantitative SILAC proteomics. Proteomic experiments were performed with HDFs as outlined in **a**. The table lists representative examples of splicing factors that participate in distinct snRNP complexes and their chromatin association in response to UV irradiation (20 J m^{-2} , 1 h). U2 and U5 snRNP splicing factors show significantly reduced chromatin association ($P \leq 0.05$, significance B¹⁷) and are

indicated with a cross. Significance B was calculated by estimating the variance of the distribution of all protein ratios, taking into account the dependency of the distribution on the summed protein intensity¹⁷. ND, not detected. **e**, Abundance of splicing factors in total cell lysates. Total lysates were prepared from U2OS cells that were mock-treated or UV-irradiated (20 J m^{-2} , 1 h post-irradiation) and splicing factor abundance was assayed by immunoblotting. Abundance of H2A is shown as a loading control. Right, immunoblots; left, quantification of splicing factor signal intensities normalized to H2A ($n = 3$, mean \pm s.d., one-way ANOVA/Bonferroni). **f**, UV-dependent interaction of splicing proteins with elongating RNAPII. Quiescent HDFs were prepared as outlined in **b** except that, instead of MNase digestion, chromatin was mechanically sheared. Elongating RNAPII was immunoprecipitated with an antibody that recognizes specifically the Ser2-phosphorylated RNAPII C-terminal domain (CTD) and its interaction with the U2 snRNP splicing factors SF3a1 and SF3b2 was assayed by immunoblotting.



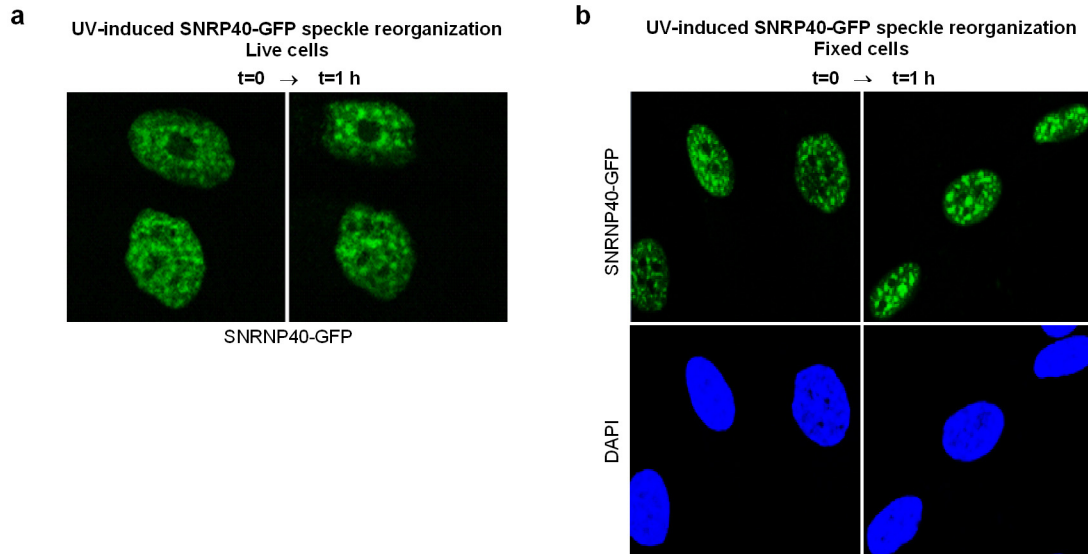
Extended Data Figure 2 | Validation of HDFs stably expressing GFP-tagged splicing factors. **a**, Whole-cell lysates from HDFs stably expressing eGFP tagged PRP8, SF3a1, SNRNP40 or free eGFP, were analysed by immunoblotting using antibodies against GFP (left) or against PRP8, SF3a1 and SNRNP40 (right). Ectopically produced proteins were expressed at near or below endogenous levels. **b**, Fluorescent microscopy images of GFP-tagged splicing factors showing the expected punctuated nuclear distribution. Images were obtained at 40 \times magnification. **c**, Localization of SNRNP40-GFP in nuclear speckles which were visualized by immunofluorescence detection of the speckle marker SRSF2/SC35. Images were obtained at 63 \times magnification. **d**, Interaction of SNRNP40-GFP with endogenous splicing factors and elongating RNAPII. Quiescent SNRNP40-GFP-expressing HDFs were mock-treated or irradiated with 20 J m⁻² UVC. After a 3-h recovery period, cells

were lysed under native conditions and chromatin was sheared by mechanical force. SNRNP40-GFP was immunoprecipitated from whole-cell lysates using GFP-Trap agarose beads, and its association with endogenous splicing factors and the large subunit of RNAPII was assayed by immunoblotting. Non-transfected cells are shown as a negative control. SNRNP40-GFP interacts with U2 and U5 snRNP components, suggesting that the GFP tag does not interfere with complex formation. Interaction of SNRNP40 with its U5 snRNP partner PRP8 is partially maintained even after MNase digestion, consistent with its presence in U4/U6.U5 tri-snRNP complexes. Participation of SNRNP40-GFP in co-transcriptional splicing complexes is confirmed by co-immunoprecipitation of the active (hyperphosphorylated RNAPII_o) large subunit of RNAPII.



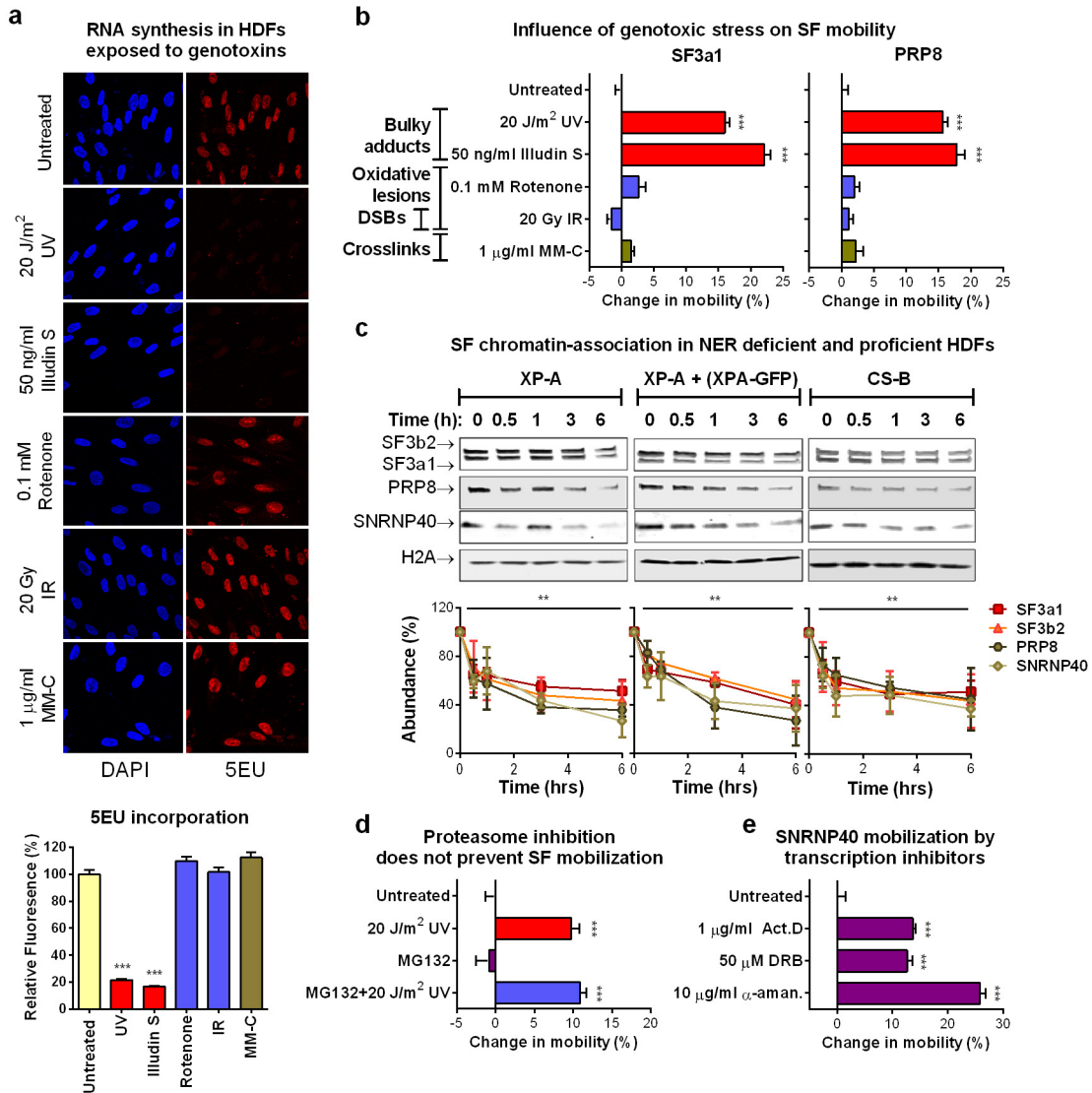
Extended Data Figure 3 | Displacement of mature spliceosomes from subnuclear sites of UV-inflicted DNA damage. **a**, U2OS cells stably expressing GFP-tagged splicing factors were UV-irradiated (60 J m^{-2}) through isopore membranes resulting in DNA lesion formation in small subnuclear areas. DNA damage sites (circled) were visualized by immunofluorescence using an antibody against the NER recognition factor XPC. Scale bar, $5 \mu\text{m}$. **b**, SF3a1-GFP and PRP8-GFP depletion from UVC laser microbeam irradiation sites. Quantification of 20 cells from two independent experiments. eGFP localization at sites of DNA damage is used to demonstrate that depletion of eGFP-tagged splicing factors is not caused by photobleaching. **c**, UVC laser microbeam irradiation results in preferential displacement of U2- and U5-associated splicing factors from DNA damage sites. Quiescent HDFs were irradiated in a $\sim 1\text{-}\mu\text{m}$ -diameter nuclear area via a UVC laser. GFP signal

intensity, reflecting the abundance of GFP-tagged U1, U2, U4 and U5 snRNP components at UVC DNA damage sites, was quantified in the irradiated and in a non-irradiated nuclear area (undamaged control). Plotted is the fluorescence signal intensity expressed as a percentage of that before irradiation, at the 1-min time point. Cells expressing free eGFP were used as negative control. Representative from three independent experiment ($n = 12$, mean \pm s.e.m., paired t -test). **d**, Depletion of splicing factors from UVC laser irradiation sites depends on active transcription. Transcription initiation was inhibited in quiescent HDFs by prolonged α -amanitin treatment ($10 \mu\text{M}$, $\geq 24 \text{ h}$) before subnuclear UVC laser irradiation. Plotted is the SNRNP40-GFP abundance in irradiated and non-irradiated nuclear areas at 1-min post-irradiation. Representative from three independent experiments ($n = 12$, mean \pm s.e.m., one-way ANOVA/Bonferroni).



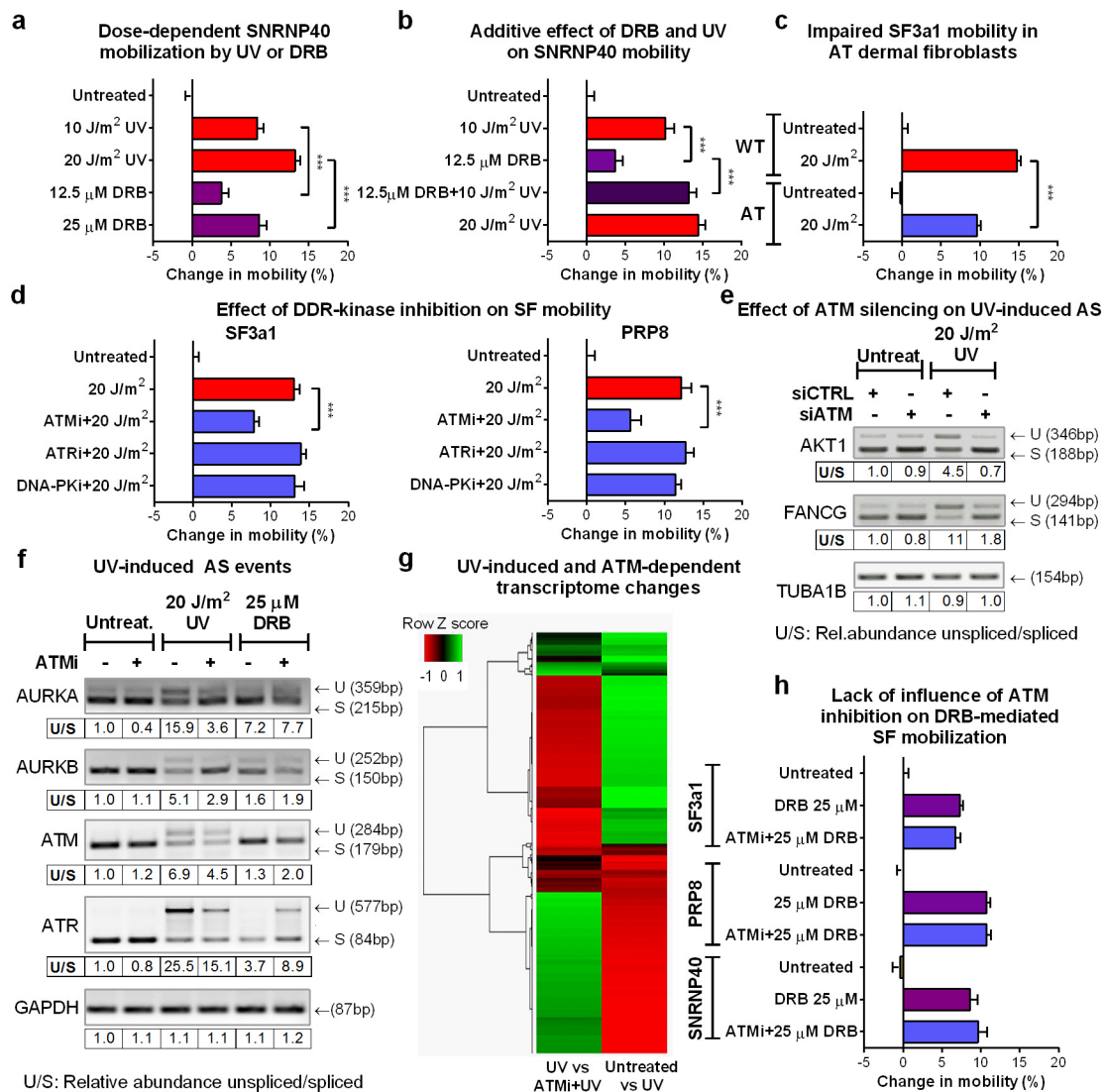
Extended Data Figure 4 | SNRP40 reorganization and speckle enlargement in response to UV irradiation. Representative microscopic images showing SNRP40-GFP distribution in quiescent HDFs before, and

1 h post UVC irradiation with 20 J m^{-2} . **a**, Live cells. **b**, Fixed cells. Images were obtained at $63\times$ magnification.



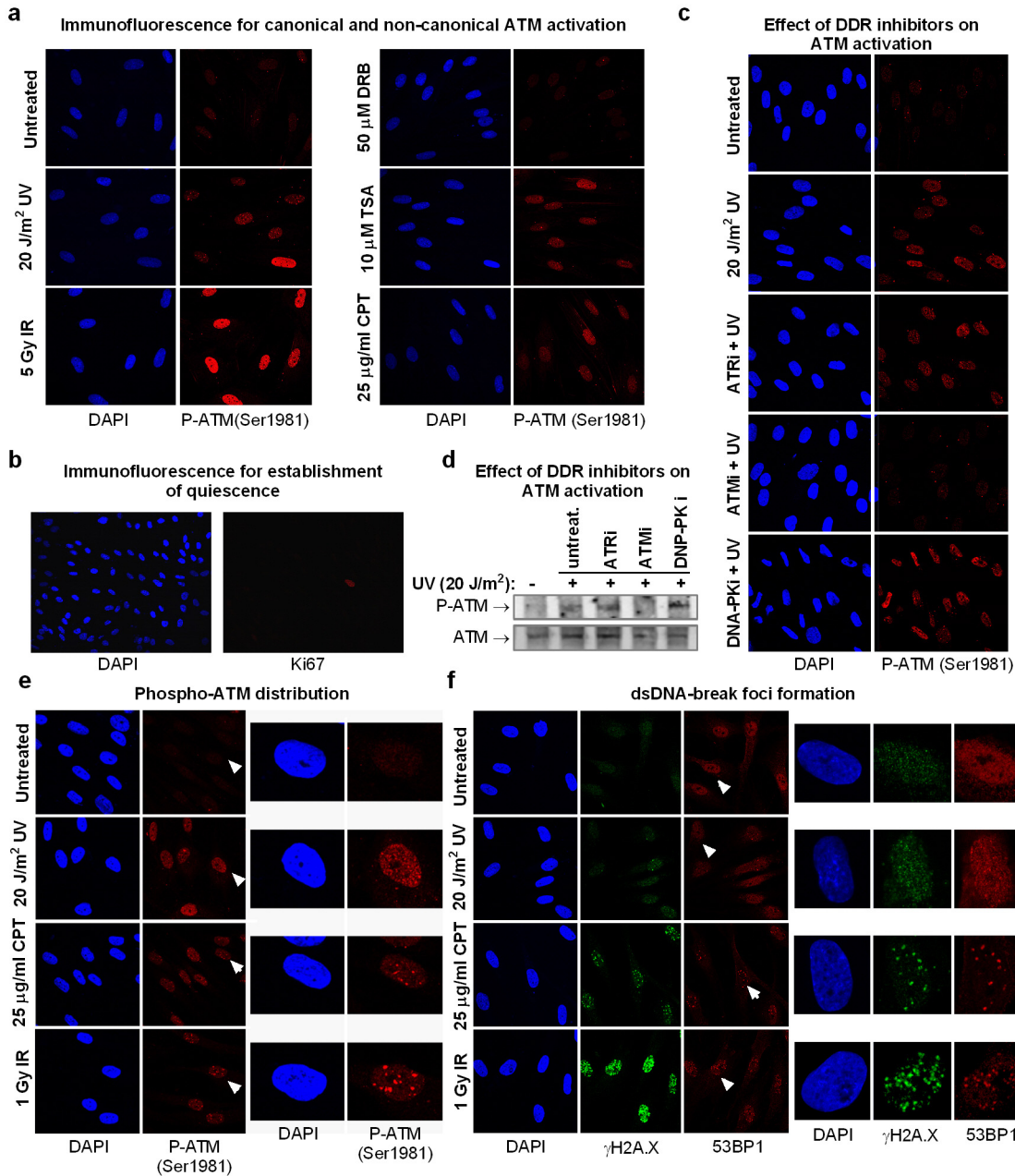
Extended Data Figure 5 | Transcription stalling mobilizes spliceosomes independent from NER complex assembly and proteasome activity. **a**, RNA synthesis is inhibited preferentially by genotoxins that inflict bulky DNA lesions. Influence of genotoxins on RNA synthesis of quiescent HDFs was measured by 5EU pulse labelling combined with click chemistry. Top, representative images; bottom, quantification of fluorescence intensity ($n = 150$, mean \pm s.e.m., one-way ANOVA/Bonferroni). Images were obtained at 40 \times magnification. **b**, Mobilization of U2 and U5 snRNPs by genotoxins inflicting transcription-blocking DNA lesions. Mobilization of GFP-tagged SF3a1 (left) and PRP8 (right) assayed by FRAP in quiescent HDFs exposed to different types of genotoxins ($n = 30$, mean \pm s.e.m., one-way ANOVA/Dunnett's). IR, ionizing radiation. **c**, Chromatin displacement of mature spliceosomes is not TC-NER-dependent. Left, chromatin abundance of U2 and

U5 snRNP splicing factors was assayed by immunoblotting in XPA-deficient (left), XPA-GFP-corrected (middle) and CSB-deficient (right) HDFs. Cells were UV-irradiated (20 J m^{-2}) and chromatin was isolated at the indicated times. Top, immunoblots; bottom, quantification of splicing factor signal intensities normalized to H2A ($n = 3$, mean \pm s.d., one-way ANOVA/Bonferroni). **d**, Proteasome activity is not required for UV-damage-induced spliceosome mobilization. Mobilization of SNRNP40-GFP assayed by FRAP in quiescent HDFs exposed to UV radiation in the presence or absence of the proteasome inhibitor MG132 ($50 \mu\text{M}$) ($n = 30$, mean \pm s.e.m., t -test). **e**, SNRNP40-GFP mobilization by transcription inhibition. FRAP of SNRNP40-GFP in quiescent HDFs after inhibition of transcription initiation ($10 \mu\text{g ml}^{-1}$ α -amanitin, 24 h) or elongation ($1 \mu\text{g ml}^{-1}$ actinomycin D or $50 \mu\text{M}$ DRB, 1 h) ($n = 30$, mean \pm s.e.m., one-way ANOVA/Dunnett's).



Extended Data Figure 6 | ATM-dependency of UV induced spliceosome mobilization, alternative splicing and gene expression changes. **a**, UV irradiation and DRB-dependent mobilization of SNRNP40. Quiescent HDFs expressing SNRNP40–GFP were UV-irradiated or DRB treated with doses that inhibit transcription to similar levels. Splicing factor mobility was assayed by FRAP. **b**, Additive effect of combined UV and DRB treatments. FRAP of SNRNP40–GFP in quiescent HDFs treated with DRB, UV, or a combination of both, each at a dose that inhibits RNA synthesis by ~50%. **c**, Impaired UV-dependent SF3a1 mobilization in cells lacking ATM activity. SF3a1–GFP mobilization was measured by FRAP in quiescent HDFs derived from an ataxia telangiectasia (AT) patient or a healthy donor. **d**, ATM-dependent spliceosome mobilization. Quiescent HDFs were treated with 10 μM ATM (KU55933), ATR (VE821) or DNA-PK (NU7441) inhibitors before irradiation. GFP-tagged SF3a1 or PRP8 mobility was assayed by FRAP. ATM, but not ATR or DNA-PK inhibition partially prevented the UV-induced splicing factor mobilization. **a–d**, $n = 25$, mean \pm s.e.m., one-way ANOVA/Bonferroni. **e**, Reduced UV-induced intron retention in response to ATM silencing. Intron inclusion in

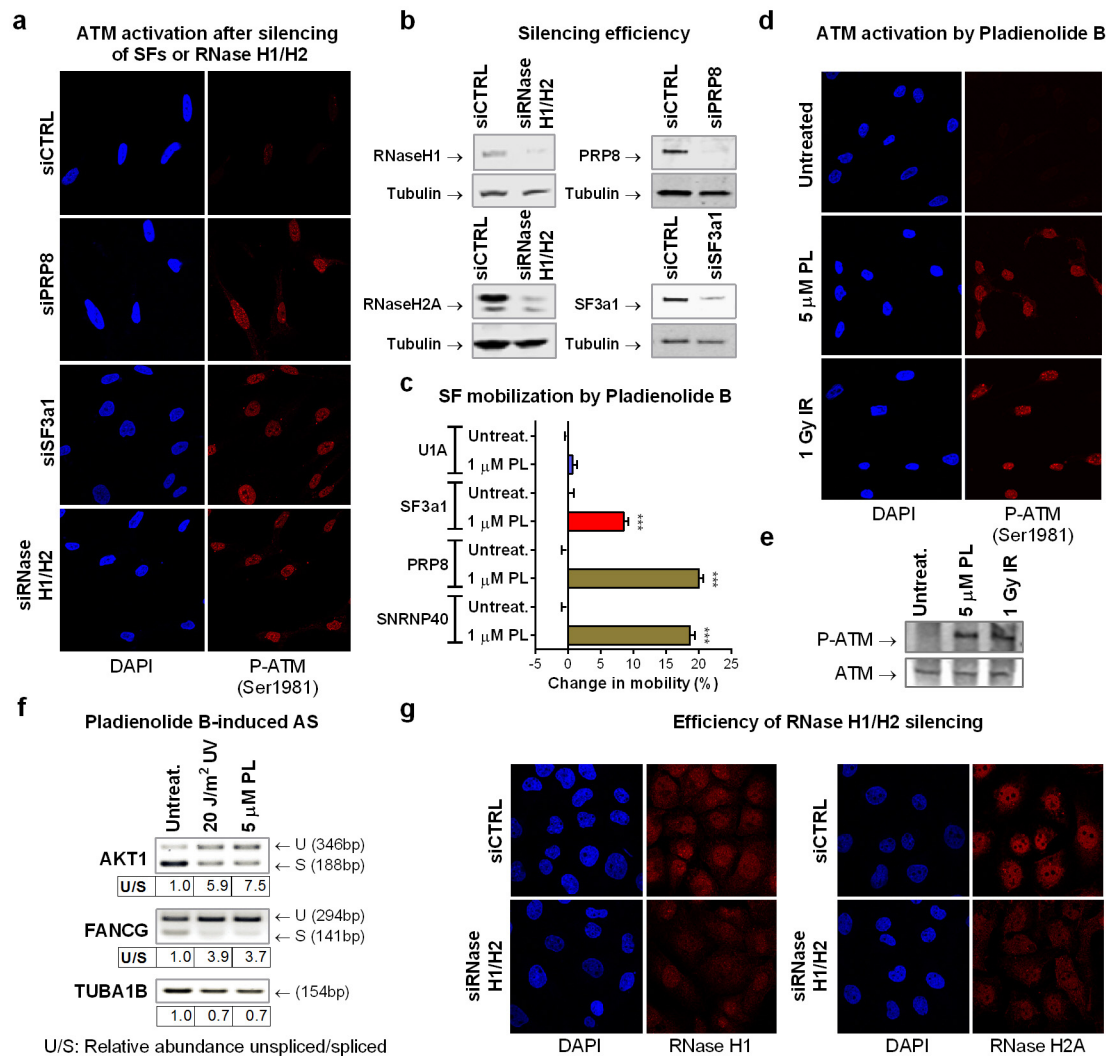
retina pigment epithelium (RPE) cells transfected either with control or ATM-silencing siRNAs and subsequently mock-treated or UV-irradiated (20 J m⁻², 6 h) was assayed by RT–PCR. **f**, ATM-dependent changes in intron retention. Intron inclusion was assayed by RT–PCR in untreated, UV-irradiated and DRB-treated quiescent cells in the presence or absence of 10 μM ATM inhibitor. **g**, Heat map of UV-triggered and ATM-dependent transcriptome changes. Quiescent cells were mock-treated or UV-irradiated in the presence or absence of the ATM inhibitor. Transcriptome profiles were generated by RNA-seq. Differentially expressed genes between untreated and UV-irradiated cells ($P < 0.05$) and UV-irradiated cells in the presence or absence of the ATM inhibitor ($P < 0.05$), were clustered in a heat map using Pearson correlation. $n = 1,676$ differentially expressed transcripts. The observed correlation indicates that UV-inducible transcriptome changes can be, in part, prevented by ATM inhibition. **h**, Lack of influence of ATM inhibition on DRB-dependent splicing factor mobility. Splicing factor mobility was measured by FRAP in untreated or DRB-treated HDFs in the presence or absence of 10 μM ATM inhibitor ($n = 30$, mean \pm s.e.m., one-way ANOVA/Bonferroni).



Extended Data Figure 7 | Canonical and non-canonical ATM activation.

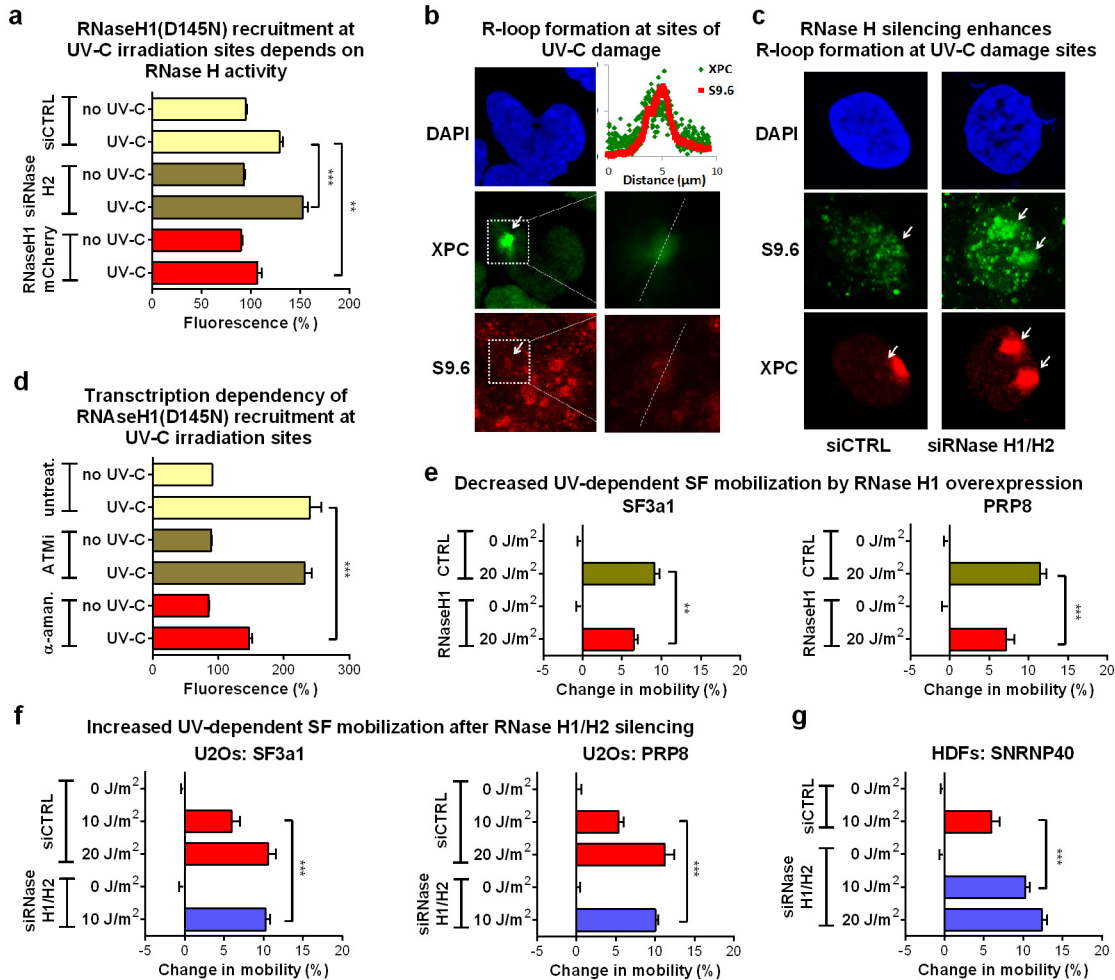
a, ATM autophosphorylation (Ser1981) was assayed in quiescent HDFs 1 h after the indicated treatments. In non-replicating cells UV and trichostatin A (TSA) activate ATM via non-canonical pathways. Transcription inhibition by DRB has no influence on ATM activity. **b**, The quiescent status of serum-deprived HDFs was verified by immunodetection of the cell cycle marker Ki67, which is not expressed by quiescent (G₀) cells. **c**, Immunofluorescence detection of active ATM in quiescent HDFs treated with DDR kinase inhibitors. **d**, Immunoblotting analysis of nuclear extracts derived from quiescent HDFs treated as in **c** using a phospho-specific ATM (Ser1981) antibody (top) and an antibody recognizing ATM (bottom). **e**, Differences in autophosphorylated-ATM distribution in quiescent HDFs treated with various ATM activators. Left,

multiple cells; right, single-cell magnification illustrating pan-nuclear localization of phosphorylated ATM after UV irradiation and focal accumulation after CPT or ionizing radiation treatments. Magnified cells are indicated by arrows (left panel). **f**, Differences in amounts of DNA damage-foci formation indicative of DSBs, in response to CPT, UV and ionizing radiation. Quiescent HDFs were pre-treated with the ATR inhibitor (10 μM, 1 h) and subsequently exposed to the indicated genotoxins. DSB foci were visualized by immunofluorescence using antibodies against γH2AX and p53BP1. Left, multiple cells; right, single-cell magnification; images were obtained at 40× and 63× magnification, respectively. Magnified cells are indicated by arrows in the left panel.



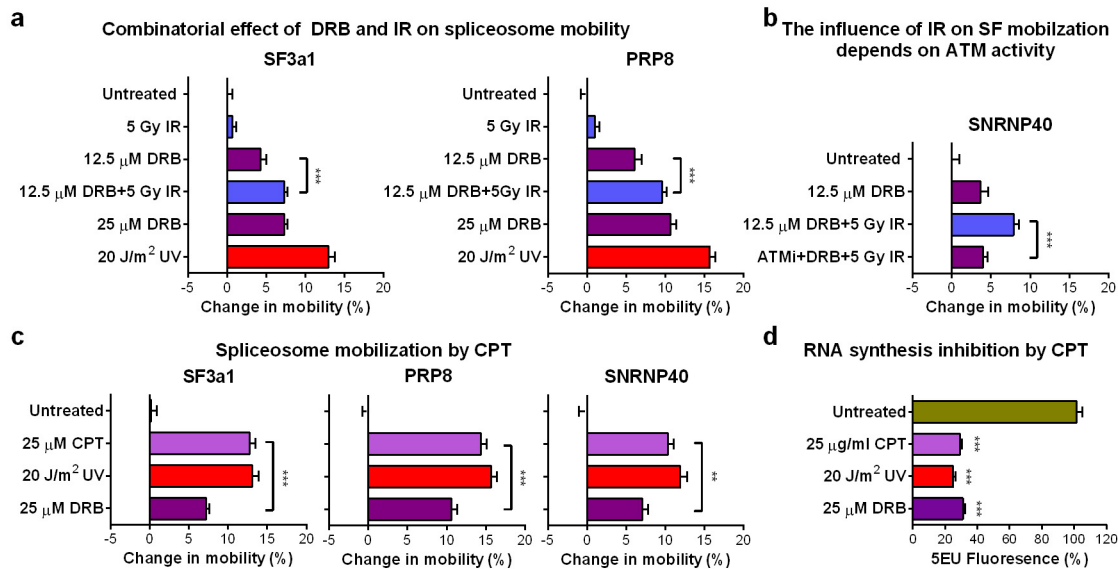
Extended Data Figure 8 | ATM activation by interference with spliceosome assembly or RNaseH1/H2A silencing. **a**, ATM autophosphorylation was assayed by immunofluorescence in HDFs after silencing of SF3a1, PRP8 or combined silencing of RNaseH1 and RNaseH2A. **b**, Immunoblotting analysis of silenced proteins in total cell lysates. Tubulin is shown as a loading control. **c**, Splicing factor mobilization by the spliceosome inhibitor pladienolide B (PL) was assayed by FRAP in quiescent HDFs. Consistent with its function in interfering with spliceosome maturation following pre-spliceosome assembly, cell treatment with pladienolide B resulted in extensive mobilization of U5 snRNP factors (PRP8 and SNRNP40), partial mobilization of the U2 snRNP SF3a1, and had no influence on the U1 snRNP factor U1A ($n = 30$,

mean \pm s.e.m., one-way ANOVA/Bonferroni). **d, e**, ATM activation by Pladienolide B. Quiescent HDFs were either treated with 5 μ M pladienolide B or exposed to 1 Gy ionizing radiation (IR) and autophosphorylated ATM was detected by immunofluorescence (**d**) or immunoblotting (**e**). **f**, Effect of pladienolide treatment on intron retention. RNA isolated from mock-treated, UV-irradiated or pladienolide B-treated RPE cells. Intron retention, as assayed by RT-PCR on transcripts of the indicated genes, shows that pladienolide B influences splicing to the same extent as UV irradiation. U/S, ratio of relative abundance of unspliced (U) to spliced (S) introns. **g**, Efficiency of RNaseH1 and H2A silencing at the single-cell level, assayed by immunofluorescence. Images were obtained at 40 \times magnification.



Extended Data Figure 9 | UV-induced R-loop formation enhances spliceosome mobilization. **a**, Recruitment of RNaseH1(D145N)-GFP at local DNA damage sites depends on endogenous levels of RNaseH activity. DNA damage was inflicted via a UVC laser in $\sim 1\text{-}\mu\text{m}$ -diameter subnuclear areas of cells after silencing of RNaseH2A or overexpression of RNaseH1-mCherry. Recruitment of RNaseH1(D145N)-GFP at the irradiated sites was monitored by live-cell imaging. Plotted is the fluorescence intensity of RNaseH1(D145N)-GFP at 1 min post-irradiation, at the irradiated and in a non-irradiated nuclear area. Representative from three independent experiments ($n = 10$, mean \pm s.e.m., one-way ANOVA/Bonferroni). **b**, **c**, R-loop formation at sites of local UVC laser irradiation. Immunofluorescence detection of R-loops using the DNA-RNA hybrid-specific S9.6 antibody. Sites of irradiation are visualized by XPC immunodetection. **b**, Dashed boxes indicate the magnified areas shown in the right panels. The dashed lines indicate the line-scan track used to quantify fluorescence intensity of S9.6 and anti-XPC (shown in the graph). **c**, Specificity of the antibody was confirmed by its increased sensitivity after RNaseH2A silencing and its ability to detect R-loops when suboptimal doses of

UVC irradiation were applied. **d**, RNaseH1 accumulation at local DNA damage sites depends on active transcription but not ATM activity. Transcription initiation was inhibited in quiescent HDFs by α -amanitin ($10\ \mu\text{g ml}^{-1}$, 24 h) before local UVC laser irradiation. Plotted is the fluorescence intensity at 1 min post-irradiation of RNaseH1(D145N)-GFP at the irradiated area and in a non-irradiated nuclear area for untreated, ATM-inhibitor- and α -amanitin-treated cells. Representative from three experiments ($n = 10$, mean \pm s.e.m., one-way ANOVA/Bonferroni). **e**, RNaseH1 overexpression inhibits the UV-dependent spliceosome mobilization. FRAP of U2OS cells stably expressing GFP-tagged SF3a1 and PRP8 and transiently transfected with RNaseH1-mCherry. **f**, RNaseH1 and H2A silencing potentiates the UV-dependent spliceosome mobilization. RNaseH1 and H2 were silenced in U2OS cells expressing SF3a1-GFP or PRP8-GFP and splicing factor mobility was assayed by FRAP. **g**, FRAP of SNRNP40-GFP in quiescent HDFs after RNaseH1/H2 silencing. **e-g**, $n = 30$, mean \pm s.e.m., one-way ANOVA/Bonferroni.



Extended Data Figure 10 | Combined transcription inhibition and ATM activation results in extensive mobilization of mature spliceosomes.

a, Combinatorial effect of DRB and ionizing radiation on spliceosome mobilization. Quiescent HDFs were exposed to ionizing radiation in the presence or absence of DRB, and SF3a1-GFP and PRP8-GFP mobility was assayed by FRAP. **b**, The ionizing-radiation-mediated increase of DRB-dependent spliceosome mobilization depends on ATM activity. FRAP of GFP-tagged SNRNP40 in quiescent HDFs treated with DRB and/or ionizing radiation in the presence or absence of an ATM inhibitor. **c**, Spliceosome

mobilization by CPT. Quiescent HDFs were treated with 25 μ g ml⁻¹ CPT, 25 μ M DRB and 20 J m⁻² UV at doses that inhibit transcription to approximately 30% and their influence on SF3a1, PRP8 and SNRNP40 mobilization was measured by FRAP. Mobilization of GFP-tagged SF3a1, PRP8 and SNRNP40 in quiescent HDFs was measured by FRAP. **a-c**, $n = 30$, mean \pm s.e.m., one-way ANOVA/Bonferroni. **d**, Inhibition of RNA synthesis by the treatments shown in **c** was assayed in quiescent HDFs by 5EU incorporation and click chemistry ($n = 150$, mean \pm s.e.m., one-way ANOVA/Dunnett's).